

PAPER

Multiscale modelling of the interaction of hydrogen with interstitial defects and dislocations in BCC tungsten

To cite this article: A. De Backer *et al* 2018 *Nucl. Fusion* **58** 016006

View the [article online](#) for updates and enhancements.

Related content

- [Hydrogen accumulation around dislocation loops and edge dislocations: from atomistic to mesoscopic scales in BCC tungsten](#)

A De Backer, D R Mason, C Domain *et al.*

- [A review of modelling and simulation of hydrogen behaviour in tungsten at different scales](#)

Guang-Hong Lu, Hong-Bo Zhou and Charlotte S. Becquart

- [Trapping of hydrogen and helium at dislocations in tungsten: an ab initio study](#)

A. Bakaev, P. Grigorev, D. Terentyev *et al.*

Recent citations

- [Predictive model of hydrogen trapping and bubbling in nanovoids in bcc metals](#)

Jie Hou *et al*

- [First-principles study of hydrogen diffusion and self-clustering below tungsten surfaces](#)

L. Yang and B. D. Wirth

- [\$\langle 001 \rangle\$ edge dislocation nucleation mechanism of surface blistering in tungsten exposed to deuterium plasma](#)

Wangguo Guo *et al*

Multiscale modelling of the interaction of hydrogen with interstitial defects and dislocations in BCC tungsten

A. De Backer¹, D.R. Mason¹, C. Domain², D. Nguyen-Manh^{1,5},
M.-C. Marinica³, L. Ventelon³, C.S. Becquart⁴ and S.L. Dudarev^{1,5}

¹ CCFE, UK Atomic Energy Authority, Culham Science Centre, Abingdon, Oxfordshire OX14 3DB, United Kingdom

² EDF Lab Les Renardières, Dpt MMC, F-77250 Moret sur Loing, France

³ DEN-Service de Recherches de Métallurgie Physique, CEA, Université Paris-Saclay, F-91191, Gif-sur-Yvette, France

⁴ Univ. Lille, CNRS, INRA, ENSCL, UMR 8207, UMET, Unité Matériaux et Transformations, F-59000, Lille, France

⁵ Department of Materials, University of Oxford, Parks Road, Oxford, OX1 3PH, United Kingdom

E-mail: andree.de.backer@ukaea.uk

Received 24 March 2017, revised 10 September 2017

Accepted for publication 21 September 2017

Published 6 November 2017



Abstract

In a fusion tokamak, the plasma of hydrogen isotopes is in contact with tungsten at the surface of a divertor. In the bulk of the material, the hydrogen concentration profile tends towards dynamic equilibrium between the flux of incident ions and their trapping and release from defects, either native or produced by ion and neutron irradiation. The dynamics of hydrogen exchange between the plasma and the material is controlled by pressure, temperature, and also by the energy barriers characterizing hydrogen diffusion in the material, trapping and de-trapping from defects. In this work, we extend the treatment of interaction of hydrogen with vacancy-type defects, and investigate how hydrogen is trapped by self-interstitial atom defects and dislocations. The accumulation of hydrogen on dislocation loops and dislocations is assessed using a combination of density functional theory (DFT), molecular dynamics with empirical potentials, and linear elasticity theory. The equilibrium configurations adopted by hydrogen atoms in the core of dislocations as well as in the elastic fields of defects, are modelled by DFT. The structure of the resulting configurations can be rationalised assuming that hydrogen atoms interact elastically with lattice distortions *and* that they interact between themselves through short-range repulsion. We formulate a two-shell model for hydrogen interaction with an interstitial defect of any size, which predicts how hydrogen accumulates at defects, dislocation loops and line dislocations at a finite temperature. We derive analytical formulae for the number of hydrogen atoms forming the Cottrell atmosphere of a mesoscopic dislocation loop or an edge dislocation. The solubility of hydrogen as a function of temperature, pressure and the density of dislocations exhibits three physically distinct regimes, dominated by the solubility of hydrogen in a perfect lattice, its retention at dislocation cores, and trapping by long-range elastic fields of dislocations.

Keywords: hydrogen, fusion, dislocation, density functional theory, linear elasticity, Cottrell atmosphere, solubility

(Some figures may appear in colour only in the online journal)

1. Introduction

Hydrogen is present in many environments, where it penetrates into metals, diffuses, forms hydrides or gets trapped at defects and dislocations in the microstructure, and at grain boundaries or interfaces between precipitates and the matrix. The mechanical properties of materials can be strongly affected by the presence of hydrogen through a phenomenon known as hydrogen embrittlement. A closely related issue, particularly pertinent to fusion, is tritium retention. This is a major challenge in the field of fusion technology [1] since it affects the safety of operation, as tritium is radioactive, and is significant in the context of tritium self-sufficiency, because a fusion power plant is expected to produce its own tritium.

The amount of hydrogen dissolved in a metal as a function of temperature and external pressure is given by the solubility law derived in [2]. Experimental measurements of hydrogen solubility by Frauenfelder [3] and other groups were reviewed recently in [4], but the data span only the high temperature interval from 1100 K to 2400 K. The solubility of hydrogen in tungsten is low, but it increases with temperature, in agreement with the positive value of solubility energy of 1.04 eV [3], which is close to theoretical predictions [5]. Defects and impurities are believed to introduce sites with lower solubility energies. According to [4], the solubility of hydrogen in a W-5% rhenium alloy, measured by Benamati at temperatures close to 850 K, is more than one order of magnitude higher than what is expected from the extrapolation of Frauenfelder's expression [3]. So far, it remains unclear whether the difference comes from the presence of rhenium or from structural defects that trap hydrogen at this relatively low temperature. Rhenium-vacancy clusters formed under irradiation [6] may provide additional traps for hydrogen.

Various models for hydrogen retention assume that it is confined at point static traps characterized by a single value of binding (or trapping) energy [7]. Release of hydrogen from traps is thermally activated. In a thermal desorption spectroscopy (TDS) experiment, the outgassing curve exhibits a peak at a characteristic temperature. It is possible to establish a linear relation between the trapping energy and the peak temperature of desorption, where the proportionality coefficient depends mainly on the temperature ramp [8]. In this work, we extend the treatment beyond the assumption of point traps, and describe interaction of hydrogen with self-interstitial type defects and dislocations. Self-interstitial defects also form dislocation loops, which are characterized by a range of trapping energies [9] and may accumulate many hydrogen atoms. Hydrogen may form dense atmospheres around dislocation loops, creating extensive traps similar in their capacity to vacancy clusters [10]. This may prove particularly significant in tungsten, where large dislocation loops can be generated during cascade collapse [11, 12].

Theoretical calculations describing the interaction of hydrogen with screw and edge dislocations have been reported in [13–16] for W and in [17, 18] for Fe. Hydrogen at dislocations in cold-worked steel has been experimentally studied in [19], and hydrogen accumulation on dislocations has been also studied in Pd [20]. The hydrogen interaction with defect

in metals is an example of solute-defect interaction. In [21], a comparison of atomistic approach and the elasticity theory revealing that the anisotropy due to the distortion induced by the interstitial carbon in iron must be taken into account. In the framework of thermodynamics for solute-defect interaction [22, 23], Kirchheim developed a theoretical approach and gave an experimental validation of hydrogen segregation on extended defects like grain boundaries, dislocation and vacancies. Hydrogen segregation on dislocations changes their mobility [24, 25] and consequently, the mechanical properties of the material. Still, the general availability of DFT data for the case of interaction of hydrogen with self-interstitial type defects in tungsten is scarce [26].

In [27], ranges of binding energies associated with the interaction between hydrogen and interstitial defects and dislocation loops, and hydrogen interacting with vacancy type defects, were deduced from TDS experiments. Binding energies in the interval from 0.4 eV to 0.8 eV were attributed to interstitial type defects. Our theoretical analysis given below broadly supports this interpretation.

In the studies of deuterium retention in tungsten, two main aspects of the retention phenomenon were identified:

On the one hand, exposure of tungsten to a deuterium plasma of low energy at high flux and high dose reveals that traps are created and modified as exposure to plasma increases, producing blisters [28, 29] and a high density of dislocations [30]. Nano-bubbles formed in the vicinity of dislocation lines are assumed [14] to serve as precursors for blisters. This conclusion is supported by simulations reported in [31] and [32].

On the other hand, in self-ion-irradiated [33] and neutron-irradiated tungsten [34], both vacancy and interstitial defects form, and as a result it is the interplay between these defects that controls hydrogen retention. A recent review of progress in modelling irradiated tungsten can be found in [35]. In [36], it was found that dislocation loop density and deuterium retention in self-ion irradiated tungsten were correlated. A comparison between ion- and neutron-damaged material also shows that a simple estimate based on the total irradiation dose does not capture all the hydrogen retention features, suggesting that evolution of defect microstructure as a function of time and temperature plays a significant part in the dynamics of hydrogen retention and release. Indeed, TDS experimental data exhibit a larger and broader desorption peak, extending to 1000 K in the cases where the material was neutron irradiated, as compared to ion damaged material for the equivalent dose. A model developed by Merrill *et al* [37] for interpreting such observations assumed a distribution of binding energies but the nature of the traps was not clarified. Microstructure was assumed to remain static even though its evolution with temperature has been demonstrated in work by Shimada *et al* [38]. When temperature increases, defects move, recombine, form clusters and loops, or are eliminated at interfaces. These processes change the concentration and nature of hydrogen traps. Ferroni *et al* [39] showed that dislocations and defects produced by the exposure of tungsten to 2 MeV self-ions evolve as functions of time and temperature. A large density of dislocation loops was observed by transmission electron microscopy, but this density diminished by a factor of three

in the temperature interval from 500 °C to 800 °C, suggesting that microstructural evolution also occurs in hydrogen desorption TDS experiments.

Models, such as HIM [40], MHIMS-reservoir [41] and TESSIM-X [42, 43] can describe hydrogen retention in an evolving microstructure in W. The models distinguish between hydrogen retention in vacancy and interstitial defect types. A suitable description of vacancy defect properties derived from DFT calculations is given in [5, 26, 44–48]. Results of atomic simulations performed using empirical potentials are given in [49–51]. The available values of binding energy of a hydrogen atom to interstitial defects relies mainly on studies of single configurations of a hydrogen atom interacting with a self-interstitial atom (SIA) defect, see [5, 52].

Schmid *et al* [42, 43] have made significant advances in the development of models for isotopic exchange, highlighting the role of weakly bound sites associated with saturable traps. An apparent synergy between deuterium retention and defect generation and evolution was reported in [53]. In [54], desorption of hydrogen was triggered by plastic deformation and the associated motion of dislocations. Also, a strong reduction of hydrogen diffusivity was predicted in the high hydrogen concentration limit [55].

Here we investigate how hydrogen interacts with interstitial type defects and dislocations. After this introduction, the second section of the paper is an atomistic study of the interaction of hydrogen atoms with interstitial defects, using DFT and empirical potentials. First, we study in detail the interaction of an H atom with a single self-interstitial atom (SIA) defect. Secondly, we decorate a single SIA with several H atoms. We consider the short-range repulsion between pairs of hydrogen atoms, and investigate the formation of a hydrogen atmosphere containing twelve or more hydrogen atoms. In the final part of the second section, we consider the interaction of an H atom with small SIA clusters, interstitial loops and a screw dislocation.

In the third section, we develop a practical multiscale modelling approach informed and parameterized by the atomistic study. Firstly, we develop a two-shell pairwise model. Assuming thermodynamic equilibrium conditions, we derive an estimate for the number of hydrogen atoms trapped by an mSIA defect as a function of temperature, and hydrogen concentration in a perfect lattice, treating it as a hydrogen reservoir for the Cottrell atmospheres [56] of defects and dislocations. Secondly, we derived analytical formulae describing hydrogen retention by an interstitial dislocation loop and an edge dislocation. This also includes a simple regularizing procedure describing the interaction between the hydrogen atmosphere and the core of a defect or a dislocation. In the final part of the third section, we show how the analytical solutions give simple and tractable expressions for hydrogen solubility in a metal in the presence of defects. The first regime, corresponding to the high temperature (or low concentration) limit and conditions characterizing Frauenfelder's experiments [3], hydrogen retention is dominated by its solubility in the perfect lattice. The second, intermediate, regime is where hydrogen is trapped only very close to the dislocation cores,

and where elastic fields play a minor role. Tungsten has such a high hydrogen solubility energy that elastic trapping around defects and dislocations is unlikely to be observable under equilibrium conditions. At the same time, plasma loading may raise the background hydrogen concentration sufficiently high, and in this case a significant amount of hydrogen may be temporarily retained in the form of dense Cottrell atmospheres around dislocations. The third regime is the low temperature (or high concentration) limit, where there is significant trapping of hydrogen in the form of Cottrell atmospheres, trapped at dislocation cores and by elastic fields of dislocations.

The last section of this paper addresses the range of validity of our models. The models show that trap mutation, in the form of spontaneous ejection of a vacancy from an interstitial defect, is *not* energetically favourable, even in the core of a large dislocation loop. We also investigate changes in the electronic charge density around 1H.1V, 1H.1SIA and 12H.1SIA hydrogen-defect complexes, which show that the accumulation of H atoms at defects is well described by the two-shell model.

2. Atomic scale models

In this section we compute binding energies characterizing the interaction between hydrogen atoms and self-interstitial atom defects, small self-interstitial atom clusters and dislocation loops, at 0 K, using density functional theory. We compare *ab initio* results with similar calculations performed using empirical potentials (EP).

2.1. Interaction of an H atom with a single self-interstitial atom

In an otherwise perfect bcc tungsten lattice, DFT calculations show that a hydrogen atom occupies a tetrahedral (1/4, 1/2, 0) site, with the formation energy of +0.95 eV, rising to 1.09 eV if the zero-point energy (ZPE) corrections are included [5, 45]. This value is in agreement with Frauenfelder's experimentally measured value of 1.04 ± 0.17 eV [3]. Because of this strongly endothermic dissolution energy, in the absence of strongly-binding traps, hydrogen concentration in bulk tungsten is expected to be relatively low.

We start our analysis with a detailed study of interaction between a single hydrogen atom and a single SIA configuration, the $\langle 1\ 1\ 1 \rangle$ dumbbell.

In [52], we found the hydrogen-SIA binding energy $E_b(1\text{H.1SIA}) = 0.33$ eV. The binding energy is defined in [57] as

$$E_b(n\text{H.mSIA}) = nE(\text{H}) + E(\text{mSIA}) - nE_{\text{ref}} - E(n\text{H.mSIA}) \quad (1)$$

where $E(n\text{H.mSIA})$ is the energy of a supercell with n H atoms decorating an mSIA defect and $E(\text{H})$, and $E(\text{mSIA})$ and E_{ref} are the energies of supercells containing one hydrogen atom in a tetrahedral site, an mSIA defect and the perfect lattice, respectively. Here the term 'energy' refers to energy or enthalpy, depending on whether the calculation was performed assuming constant volume or constant (zero) pressure.

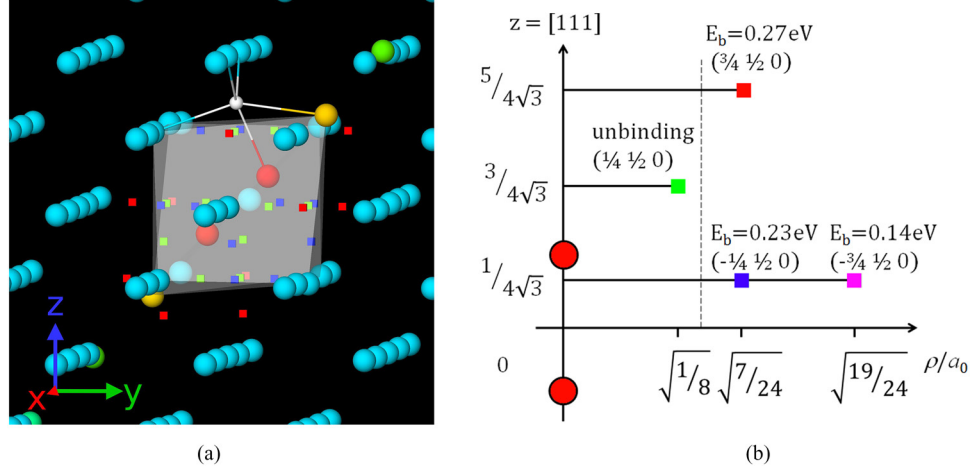


Figure 1. (a) The most stable 1H.1SIA configuration and other tetrahedral sites. The SIA defect forms the dumbbell of two red atoms encapsulated in the semi-transparent surfaces. (b) $(\pm 1/4, \pm 1/2, 0)$ and $(\pm 3/4, \pm 1/2, 0)$ sites form eight hexagonal rings evenly spaced along the z -axis with varying radii ρ , as indicated. The positions are symmetric about the $z = 0$ plane. The dashed vertical line indicates the effective ‘radius’ of the dumbbell (see equation (5)).

A 1H.1SIA configuration is shown in figure 1. A hydrogen atom sits in a cubic cell next to the one that contains the dumbbell, and the H atom has 5 nearest W atoms, one of them being one of the dumbbell. More hydrogen-dumbbell configurations have been investigated. We used VASP [58] and PBE exchange-correlation functional [59], assuming the cut-off energy of 350 eV and a $2 \times 2 \times 2$ k -points mesh. Our DFT calculations were performed at constant volume and corrected using the elastic correction scheme described in [60] with elastic constants $C_{11} = 522.8$, $C_{12} = 203.5$ and $C_{44} = 160.7$ GPa. We do not include the zero point energy corrections. The box size for the dumbbell calculations was $5 \times 5 \times 5$ unit cells, containing $250 + 1$ W atoms. Calculations with other box sizes and k -points meshes have also been carried out. The convergence of calculations will be detailed elsewhere, as it does not affect the development of the model reported here.

We only report binding energies for fully relaxed configurations, where the hydrogen atom is slightly displaced from ideal interstitial locations. Still, it is convenient to discuss atomic geometry in terms of ideal lattice reference sites. A hydrogen atom near a dumbbell occupies tetrahedral interstitial sites. To understand the geometry of equivalent sites and the associated binding energies, note that the 24 $(\pm 1/4, \pm 1/2, 0)$ and 24 $(\pm 3/4, \pm 1/2, 0)$ tetrahedral sites nearest to $(0, 0, 0)$, the centre of the dumbbell, form a set of eight hexagonal rings, evenly spaced along the dumbbell axis, with varying radii ρ , as illustrated in figure 1(b) (and also indicated by small coloured cubes in figure 1(a)). The smallest rings with $\rho = a_0/\sqrt{8}$ (where a_0 is the lattice parameter) contain twelve non-binding sites (green cubes). The rings at $\rho = a_0\sqrt{7/24}$, $z = \pm a_0/4\sqrt{3}$ contain the twelve most binding sites, with $E_b(1H.1SIA) = 0.27$ eV (red cubes). The difference between this result and that quoted in [52] is due to the simulation cell size and the number of k -points grid. The rings at $z = \pm a_0/4\sqrt{3}$ contain 12 slightly weaker bound sites, with the inner rings ($\rho = a_0\sqrt{7/24}$) characterized by the binding energy of 0.23 eV (blue cubes). More

binding energies as a function of the lateral distance from the dumbbell are shown in figure 2.

The same calculations have been performed using empirical potentials. For our empirical potential calculations we used LAMMPS [61] and several potentials: the BOP potential by Juslin *et al* [62] (BOPJ), the BOP potentials by Li *et al* [63] (BOPL) and two EAM potentials by Bonny *et al* [49] (EAM1 and EAM2). These last two define W-H interactions with a common W-W interaction given by Marinica *et al* [64]. A box containing $20 \times 20 \times 20$ unit cells was used. Similarly to the DFT calculations, we used constant volume relaxation and the image elastic correction scheme [60]. Small changes in elastic constants between the potentials (see table 1) had a negligible effect on numerical results. Likewise, the variation of the elastic constants resulting from the addition of a hydrogen atom to the simulation cell had a negligible effect on the computed values.

Binding energies, computed using the empirical potentials, are given in figure 2. The BOPJ potential incorrectly places the $\langle 110 \rangle$ dumbbell 1.72 eV lower in energy than the $\langle 111 \rangle$ dumbbell, and so it has been excluded from the single dumbbell study. EAM1 correctly reproduces the maximum binding energy but underestimates interaction at long range. EAM2 overestimates the binding energy but correctly reproduces the long-range interaction, and BOPL overestimates both the binding energy and long-range interaction. We shall demonstrate in sections 3.1 and 3.2 that the long-range interaction energy is due to elastic field of the SIA defect and is proportional to the relaxation volume of a hydrogen interstitial atom.

2.2. Interaction of several H atoms with a single SIA

In the preceding section, we computed interaction between a single H atom and a single $\langle 111 \rangle$ dumbbell SIA. We showed that the D_{3d} symmetry of the dumbbell, coupled with the observation that H atoms occupy tetrahedral sites near a single

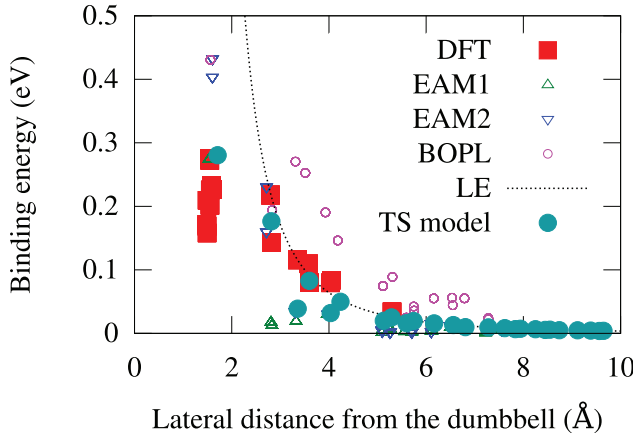


Figure 2. The binding energy of a 1H.1SIA configuration as a function of the lateral distance between an H atom and a self-interstitial dumbbell calculated using DFT, empirical potentials, linear elasticity (LE, see section 3.2) and the two-shell model (TS Model) (see section 3.1).

SIA, gives rise to hexagonal rings of equivalent sites, with the most binding four rings (twenty four sites) having the binding energy in the range $E_b \sim 0.23\text{--}0.27$ eV. To understand the multiple hydrogen and single defect configurations, we propose a decomposition of the binding energy of n H atoms to a defect into several *object pairwise* components and a *many-body* correction.

$$E_b(nH.mSIA) = \sum_{i=1}^n E_b(H^{(i)}.mSIA) + \frac{1}{2} \sum_{i=1}^n \sum_{j \neq i} E_b(H^{(i)}.H^{(j)}) + \Delta E_b(H^{(1)}.H^{(2)} \dots mSIA). \quad (2)$$

The first term is a sum of pairwise contributions made by the i th H atom and the SIA defect. The second term is a sum of H–H pairs. We now show that the many-body correction, $\Delta E_b(H^{(1)}.H^{(2)} \dots mSIA)$, is small and we neglect it in the two-shell model developed in section 3.1.

First we consider the pairwise H–H interaction. Interaction energies of H–H pairs in perfect bcc tungsten as a function of their separation distance have been reported in [52] and are summarised in table 2, together with the values computed using EPs. DFT predicts that the H–H interaction is mainly repulsive between the first nearest neighbour (1NN) and second nearest neighbour (2NN) pairs, which is reproduced by EAM1. EAM2 and BOPL predict long range repulsion, which is difficult to justify. The repulsive interaction between H atoms suggests that they would not spontaneously accumulate, unless trapped by a defect. This is different to the case of He atoms in tungsten, where He atoms exhibit clustering and self-trapping by trap-mutation [66].

Next we consider the 2H.1SIA system and equation (2) becomes

$$E_b(2H.1SIA) = E_b(H^{(1)}.1SIA) + E_b(H^{(2)}.1SIA) + E_b(H^{(1)}.H^{(2)}) + \Delta E_b(H^{(1)}.H^{(2)}.1SIA) \quad (3)$$

Table 1. Elastic constants, maximum binding energies and relaxation volumes calculated using DFT and EPs. Values of relaxation volume are reported as a multiple of atomic volume $\Omega = a_0^3/2$. The elastic constants computed using DFT are taken from [65].

	DFT	EAM1	EAM2	BOPJ	BOPL	2-shell
E_b (eV)	0.27 (0.33 ^a)	0.27	0.43	0.71	0.43	0.28
$\Omega_H^{\text{rel}}/\Omega$	0.15	0.06	0.15	0.11	0.44	0.15
C_{11} (GPa)	537.4	523	523	515	542	537.4
C_{12} (GPa)	188.2	203	203	203	191	188.2
C_{44} (GPa)	153.7	160	160	163	162	153.7
a_0 (Å)	3.17	3.14	3.14	3.16	3.16	3.165

^a 0.33 eV reported in [52] was obtained using a $3 \times 3 \times 3$ set of k -points and a 128 atom box. Our result, 0.27 eV, is for a $2 \times 2 \times 2$ set of k -points and a 250 atom box. For the two-shell model (see section 3.1) the relaxation volume and elastic constants are input parameters, and the maximum binding energy has been computed.

Table 2. H–H pair binding energy (in eV) in bcc tungsten predicted by DFT and empirical potentials. Repulsive configurations are shown in bold. The two-shell model (see section 3.1) takes H–H repulsive energies as input.

	1NN	2NN	3NN	4NN	5NN	6NN
A	A	B	C	D	E	E'
d (l.u.)	0.3	0.5	0.6	0.7	0.8	0.9
d (Å)	1.1	1.6	2	2	2.5	2.7
EAM1	−0.47	−0.16	−0.06	−0.02	−0.02	−0.02
EAM2	a	−0.11	−0.05	−0.11	−0.20	−0.14
BOPJ	−0.50	−0.14	−0.1	−0.05	−0.01	0.00
BOPL	−0.63	−0.16	−0.13	−0.19	−0.15	−0.11
DFT	−0.47	−0.11	−0.03	0.01	0.00	
2-shell	−0.47	−0.11	0	0	0	0

^a Highly unstable non-binding configuration.

where the first two terms depend on the H–SIA distances and the third term depends on the H–H distance. One H atom was placed on one of the twelve most binding sites, and a second placed in one of the other twenty-three strongly binding sites. To this systematic set, a further ten randomly generated configurations with the H atoms placed up to 3 Å from the centre of the dumbbell were added. The results are shown in figure 3. The small scatter of the points (<0.1 eV) demonstrates that we can indeed treat the many-body energy correction $\Delta E_b(H^{(1)}.H^{(2)} \dots 1SIA)$ as small compared to the pairwise energy. This demonstrates that the many-body interaction H–SIA–H is small. This is one of the key results of this work.

To identify the many-body part of the interaction, we decorated a $\langle 111 \rangle$ dumbbell with an increasing number of H atoms, varying the number of hydrogen atoms from 3 to 20. The multiplicity of arranging n hydrogen atoms on tetrahedral sites means that we cannot explore all the configurations exhaustively, and instead need to generate a sample set of atomic structures. A set of sample configurations was generated by randomly populating tetrahedral sites up to $2a_0$ from the centre of the dumbbell, then relaxing them with EAM2. The most bound configurations were then passed on to DFT

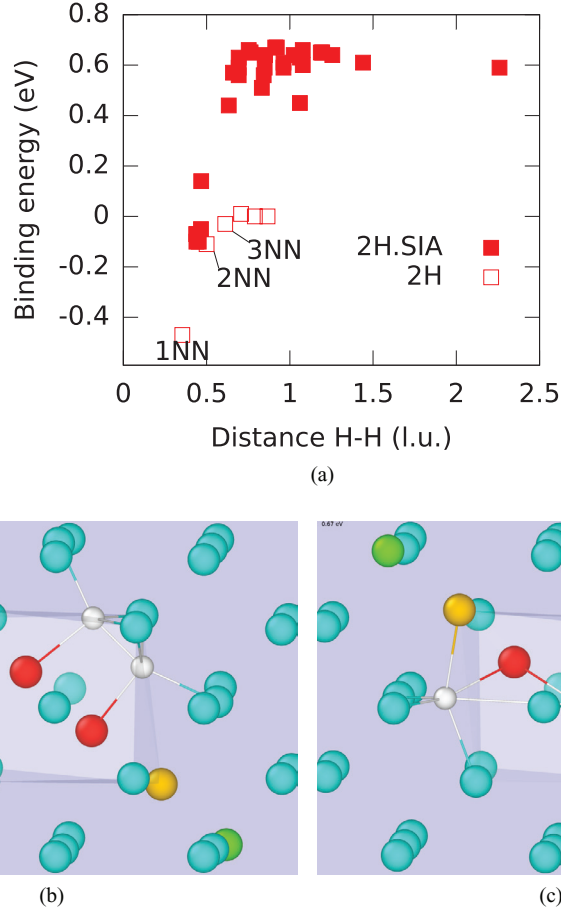


Figure 3. (a) Binding energy of a 2H pair in perfect bcc lattice and in 2H.1SIA as a function of the H–H distance after relaxation, calculated by DFT. (b) An example of an energetically unfavourable configuration where the H atoms are in the 1NN configuration. (c) An example of a binding configuration where the H–H distance is close to a_0 . The configurations are shown in the [100] projection and W atoms of the dumbbell are shown in red. Bonds are shown between H and W atoms separated by distances shorter than 2.2 Å.

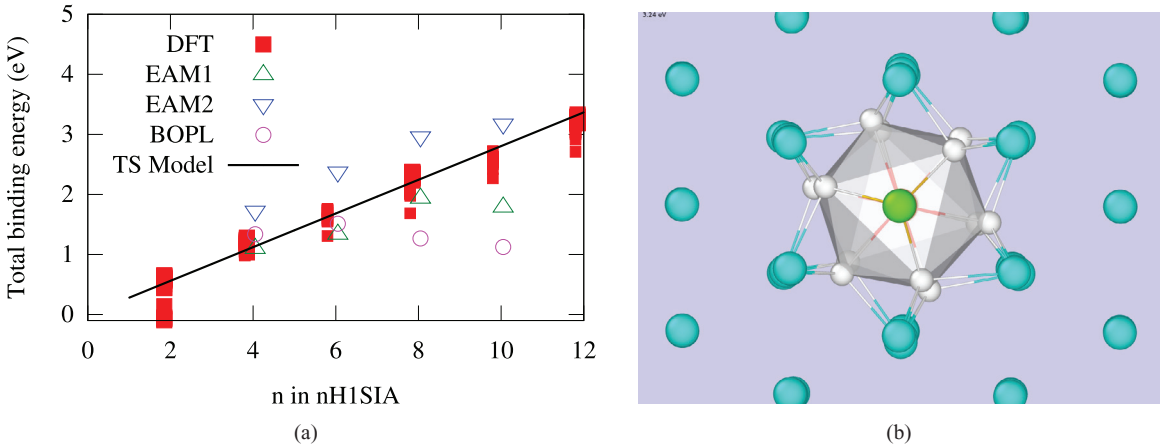


Figure 4. (a) The binding energy of $nH.1SIA$ calculated by DFT and the maximum binding energy computed using EPs. Also shown are the maximum binding configurations with our two-shell model (see section 3.1). (b) The most favourable 12H.1SIA configuration by DFT, viewed from the [111] direction. The configuration has three H atoms in each of the four most binding rings (see figure 1).

calculations. Altogether, more than 500 distinct configurations were computed with DFT. The total binding energy increases from 1.2 eV for $n = 4$ to 6 eV at $n = 20$ but exhibits significant variations depending on the configuration of H atoms around the SIA, as seen in figure 4. The effect of DFT box size and k -points will be detailed elsewhere, and has no bearing on the development of the model described here.

We supplemented the above investigation with a systematic study of a 12H.1SIA system, populating the twenty four most binding sites found in section 2.1 with all the configurations of twelve H atoms, where no pair of H atoms were in the nearest neighbour positions. The results are shown in figure 4. For 12H.1SIA, the maximum binding energy configurations are where three hydrogen atoms are added to each of the

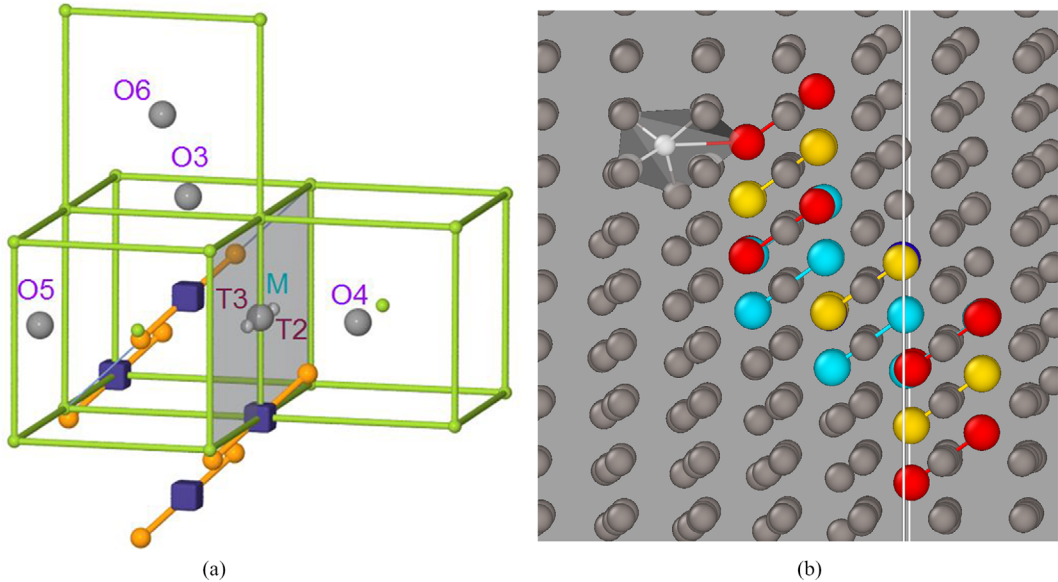


Figure 5. (a) Sketch of a 4SIA cluster studied by DFT and the positions where an H atom has been introduced to calculate the binding energies. (b) The most favourable 1H.19SIA configuration predicted by DFT. White lines show the five nearest W atoms, which are the four atoms forming the tetrahedral site plus the nearest of the two atoms of the dumbbell.

four most-binding hexagonal rings (see figure 1), with three H atoms on each ring forming an equilateral triangle. This is the only way to populate the available sites, excluding 1NN and 2NN H–H pairs. Rotating the rings varies the 12H.1SIA binding energy through 2.4 eV, 2.9 eV and 3.2 eV, with the most favourable configuration for H atoms corresponds to them being aligned along [1 1 1] rows during the relaxation. We note that the maximum binding energies computed for the n H.1SIA system with DFT increase roughly linearly with n up to $n = 12$. This further validates the fact that the many-body interaction $\Delta E_b(H^{(1)}.H^{(2)} \dots 1SIA)$ is small and that the 1NN and 2NN H–H pair exclusion also applies to n H.1SIA.

2.3. Interaction of an H atom with an mSIA defect

In this section we consider interaction between a single H atom and large *m*SIA interstitial clusters and loops, with $m = \{4, 10, 19, 37\}$. VASP calculations similar to those described in the preceding sections were used to compute the energies, but with the box size now extending up to $9 \times 9 \times 9$ unit cells to reduce box size effect. We also performed calculations using EPs.

Starting with the $m = 4$ interstitial cluster, we placed an H atom initially in either tetrahedral and octahedral interstitial sites (with respect to the ideal lattice), as illustrated in figure 5(a). Binding energies evaluated following relaxation, are summarised in table 3.

We next considered a larger $m = 10$ interstitial loop. The minimum energy configuration of the loop with a formation energy of 53 eV, according to DFT, has SIAs arranged as a 7SIA circular loop, plus 3 extra SIAs situated at points (2, 0), (1, 1) and (2, -1) in the Bravais lattice in the (1 1 1) plane (see figure 6). This loop structure is also the lowest energy configuration if computed using EPs. The energy of an H atom initially placed in each of around 6500 tetrahedral sites was computed with EPs; the result is illustrated in figures 6(a)–(c). There is

Table 3. Binding energies, in eV units, of various 1H.4SIA configurations illustrated in figure 5(a), calculated by DFT using $4 \times 4 \times 4$ atom cells and $3 \times 3 \times 3$ k -points grid.

Configuration	Binding energy
T2	0.27
O3	0.11
O5	0.26
T3	0.35
O4	0.30
O6	0.22

some variation in the maximum binding energy, for EAM1 we find 0.41 eV, for EAM2 it is 0.70 eV, for BOPL it is 0.80 eV and the position of the most bound H atoms does vary—for example, it occupies a tetrahedral site immediately beyond the loop perimeter but at the shorter side of the loop for EAM1 and EAM2 while it occupies the longer side of the loop for BOPL and DFT. As with the $\langle 1 1 1 \rangle$ dumbbell, we find that EAM1 has the shortest range and the lowest binding energy, whereas BOPL has the largest range and the greatest binding energy. We shall show in section 3.2 that this pattern is globally consistent with elastic interaction between a self-interstitial atom cluster and an H atom, even though the treatment of elastic interaction does not account for the non-circular shape of the loop.

Motivated by the empirical potential simulations, we have calculated DFT binding energies of 50 configurations where a single H atom is close to the perimeter of the cluster, as illustrated in figure 6(b). The maximum binding energy is found to be $E_b(1H.10SIA) = 0.57$ eV, when an H atom is placed at a perpendicular distance $0.6a_0$ from the centre of mass of the closest dumbbell. The binding energy decreases to 0.46 eV at $0.85a_0$ separation, and to 0.25 eV at $1.1a_0$ separation.

The same approach has been applied to larger prismatic loops using DFT and EP. A sketch of the most binding 1H.19SIA configuration (with DFT) is given in figure 5(b). An H atom is

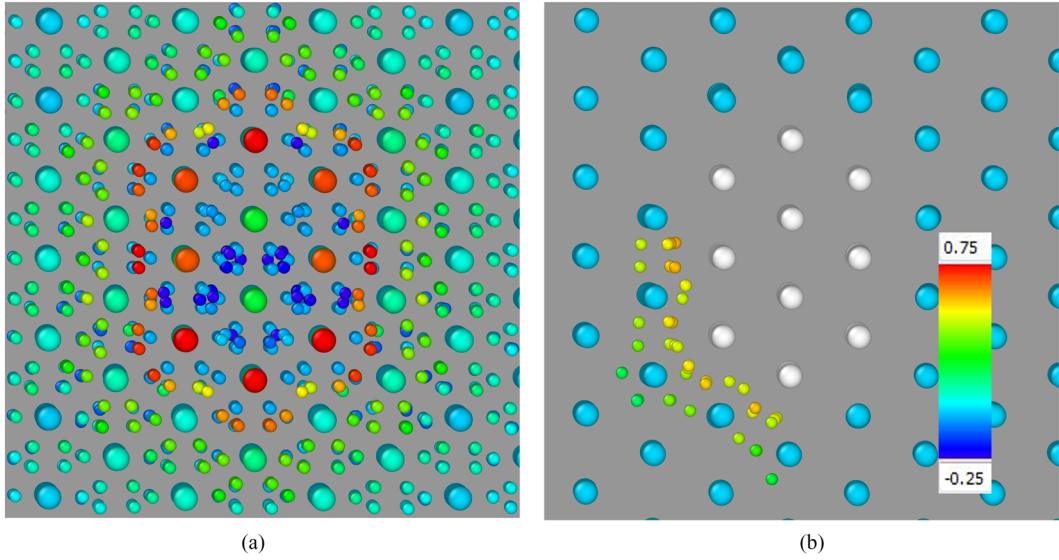


Figure 6. Map of the energy of interaction between an H atom and a 10SIA loop calculated using an empirical potential BOPL (a) and DFT (b). The structure is viewed from a [1 1 1] direction, W (resp. H) atoms are shown as large (resp. small) spheres. Colour scale from blue to red reflects the binding energy.

near the loop with 4W atoms at 1.9 Å: forming a tetrahedral site plus one W atom of the dumbbell at 2.6 Å. The maximum binding energy increases as a function of loop size, and differences between the DFT and EP values are large (see figure 7(b)). According to the DFT results, the maximum binding energy is larger for the less symmetric 10SIA loop than for a prismatic 19SIA one, but an opposing trend is predicted by the EPs. Only a small difference is visible between the cases of 19SIA and 37SIA loops, suggesting that the nature of the interaction is similar to that of hydrogen interacting with an edge dislocation. This is confirmed by the fact that the distances between an H atom and the five nearest W atoms in the most favourable 1H.19SIA configuration are essentially the same as in a 1H.37SIA.

The results suggest that the maximum binding energy increases with loop size m , with some variability due to atomic environment around the loop perimeter. The rate of increase is sublinear, and both DFT and empirical potential results support the existence of a finite limit to the binding energy at the infinite loop size, corresponding to the binding energy of an H atom to an edge dislocation line. From the DFT results, the 0.66 eV binding energy value, which is the value obtained with the $m = 37$ loop, should be close to this limit. We performed DFT calculations of the H interaction with screw dislocations and found that the maximum binding energy is 0.56 eV in agreement with [13], which is lower than the energy of hydrogen binding to an edge dislocation. We return to the edge dislocation limit, and its implications, with simplified elasticity-based models in sections 3.1 and 3.2.

3. Model for hydrogen retention on interstitial clusters and dislocations

In this section we consider the elastic interaction between an H atom and a dislocation loop, and the binding of an H atom to a dislocation core, in spatially distinct regions. We demonstrate that treating the H-defect interaction as purely elastic at

large distances is a good match to the DFT data and empirical potential results. We show where linear elasticity fails near the dislocation core, and propose a two-shell model (TS) for the interaction: elastic at long range and fitted to DFT at short range. We compute the free energy of a $nH.mSIA$ system at finite temperature using thermodynamic integration, and predict the retention of hydrogen on interstitial defects at a finite temperature. Using further approximations, we derive simple analytical expressions for the number of H trapped by dislocation loops and an edge dislocation, giving a simple expression for H solubility in tungsten as a function of temperature, pressure and the density of dislocations.

3.1. The two-shell model

The energy of interaction between a dislocation loop with a Burgers vector \mathbf{b} and a point source of dilatation at a separation \vec{R} from the centre of the loop [67] is

$$U(r, z) = \Omega_H^{\text{rel}} \frac{b\mu}{3\pi} \left(\frac{1+\nu}{1-\nu} \right) \frac{1}{D(z, r, \rho)},$$

$$D(r, z, \rho) = \frac{\sqrt{z^2 + (\rho+r)^2}}{\frac{\rho^2 - r^2 - z^2}{(\rho-r)^2 + z^2} E\left(\sqrt{\frac{4r\rho}{z^2 + (\rho+r)^2}}\right) + K\left(\sqrt{\frac{4r\rho}{z^2 + (\rho+r)^2}}\right)}, \quad (4)$$

where $b = \mathbf{b}_z$, $z = \vec{R} \cdot \hat{n}$, is the projection of the vector separation on the loop normal, $r = \sqrt{R^2 - z^2}$ is the projected distance on the plane, and $\Omega_H^{\text{rel}} > 0$ is the relaxation volume of the dilatation centre representing a hydrogen interstitial atom. $K(k)$ and $E(k)$ are elliptic integrals of the first and second kinds, respectively. We use the convention that b is positive for an interstitial loop, and for $|\vec{R}| \gg \rho$ the elliptic integrals may be Taylor expanded as

$$K(k) \approx \frac{\pi}{2} \left(1 + \frac{k^2}{4} + \frac{9k^4}{64} - \dots \right)$$

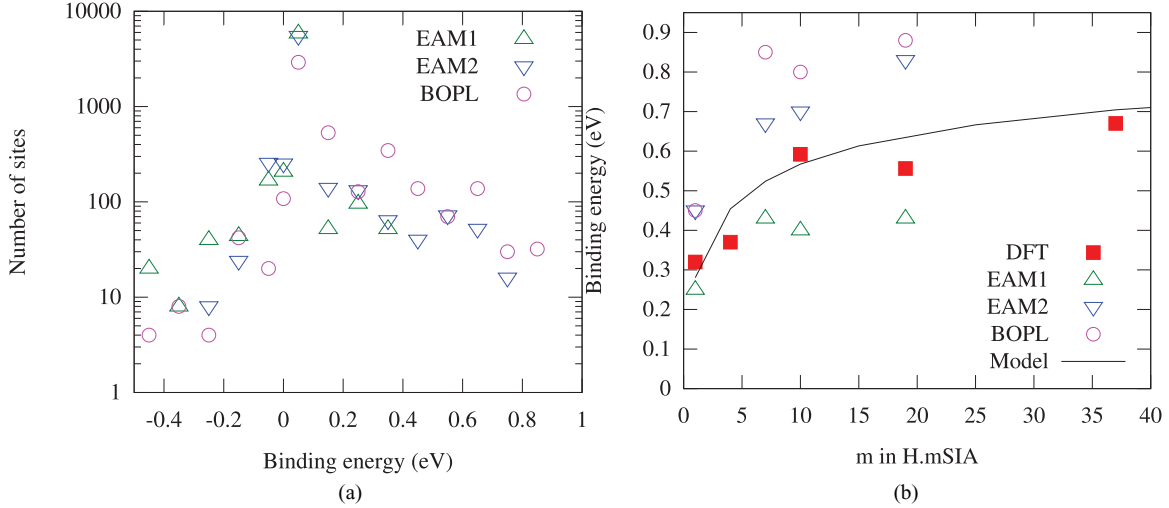


Figure 7. (a) Histogram of binding energies for an H atom in a cylinder around a 10SIA loop computed with EPs. (b) The maximum binding energy as a function of m_{SIA} and loop size with atomistic models and our two-shell model (see section 3.1).

$$E(k) \approx \frac{\pi}{2} \left(1 - \frac{k^2}{4} - \frac{3k^4}{64} + \dots \right).$$

For an interstitial loop and a point source with positive relaxation volume, such as an interstitial hydrogen atom, this interaction is attractive outside the loop and in the plane, and repulsive inside, above and below the loop. $U(r, z)$ is negative when the interaction is attractive and is the opposite value of the binding energy as defined by equation (1). Figure 8 shows contours of the binding energy of one H atom with a 55SIA (loop radius, $\rho = 1 \text{ nm}$). By anticipation, grey oblongs indicate the core-shell of the loop where another treatment will be applied.

For the radius of a circular $1/2\langle 111 \rangle$ loop containing m self-interstitials we use

$$\rho(m) = a_0 \sqrt{\frac{m}{\sqrt{3}\pi}}, \quad (5)$$

which is also well-defined in the limiting case $m = 1$.

We can use equation (4) to compute the elastic binding energy of a hydrogen atom to an interstitial dumbbell; the result is plotted in figure 2. The strength of the interaction is characterized by the constant prefactor $\frac{b\mu}{3\pi} \left(\frac{1+\nu}{1-\nu} \right)$, where $\mu = 0.99 \text{ eV } \text{\AA}^{-3}$ is the shear modulus of tungsten and $\nu = 0.28$ is its Poisson's ratio. The equations above assume that the material is elastically isotropic, which is a good approximation for tungsten. The elastic constants, to which the W-W empirical potentials included in our study are fitted, vary by at most a few percent. The computed values of the relaxation volume Ω_H^{rel} vary considerably between the empirical potentials (see table 1). EAM1 has the smallest relaxation volume $\Omega_H^{\text{rel}} = 0.06\Omega$, and has the weakest long-range interaction, whereas BOPL has the largest ($\Omega_H^{\text{rel}} = 0.44\Omega$) and has the strongest long-range interaction. EAM2 has $\Omega_H^{\text{rel}} = 0.15\Omega$, in agreement with DFT, and its long-range interaction agrees with DFT. The interaction between hydrogen and interstitial defects at long range is elastic in nature, which is confirmed by the DFT and EP.

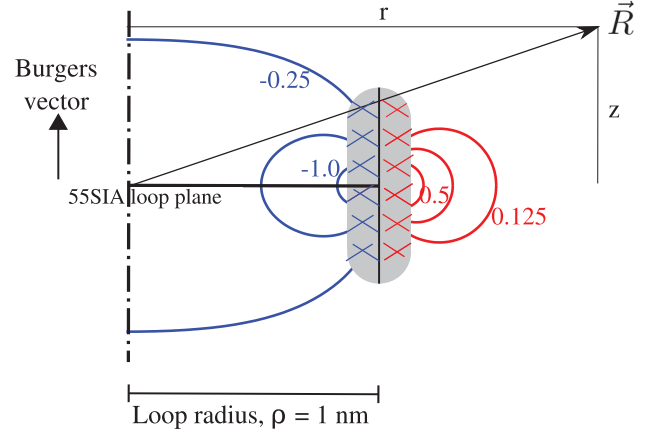


Figure 8. Contours of the binding energy of one H atom with an m_{SIA} loop, using equation (4) for $m = 55$. The plane of the $1/2\langle 111 \rangle$ loop is perpendicular to the Burgers vector shown in the figure. Note that the interaction energy has the opposite sign to the binding energy. The attractive region has positive binding energy contours, outside the loop (red lines, $E_b = \{0.125, 0.25, 0.5\} \text{ eV}$), and the repulsive region has negative binding energy contours, inside (blue lines, $E_b = \{-0.25, -0.5, -1.0\} \text{ eV}$). The grey oblongs represent the core region of the two-shell model where the binding energy is fixed (see text).

As a hydrogen atom is brought from infinity in the plane of an interstitial loop, equation (4) implies that its binding energy increases and becomes divergent on a circle of radius $\rho(m)$ aligned with the loop. This unphysical behaviour originates from the continuum elasticity approximation; the dislocation core must be handled differently. Equation (4) could be regularized, or gradient elasticity [68, 69] could be used. Because the core region concerns only a limited number of sites, our approach is to propose a simple two-shell model, with a core region close to the dislocation loop perimeter at $\rho(m)$, and linear elasticity beyond. Within the core region we constrain the binding energy to not exceed the minimum (resp. maximum) values on the outer (resp. inner) surface.

It is desirable to describe the core region with as few adjustable parameters as possible. We propose that the core

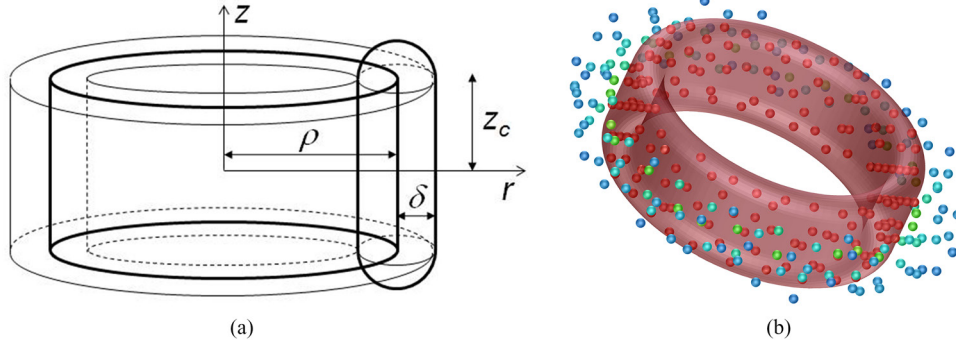


Figure 9. (a) A sketch of the geometry of the dislocation loop in our TS model. ρ is the loop radius, δ is the core or minor radius and z_c is the longitudinal extension. (b) A low energy configuration of an $m = 55$ loop ($\rho = 1$ nm) decorated with 316H atoms found by Metropolis Monte Carlo. The H atoms are coloured by binding energy; the most binding H atoms are red (0.75 eV binding energy) inside the core region, scaling through green (0.5 eV) to blue (0.1 eV) in the elastic region.

region is not simply a torus, but instead has greater extension in the direction along the Burgers vector. A fat-walled tube is obtained using a toroidal building block with major radius ρ and minor radius δ and translate it a longitudinal extent $\pm z_c$ along the loop normal. The energy of H within the core is

$$\begin{aligned} U_{\text{core}}(r, z) = \min & [U(\rho + \delta, 0), \\ & \max \{U(\rho - \delta, 0), U(r, |z| - \min(|z|, z_c))\}]. \end{aligned} \quad (6)$$

The geometry of the two-shell model is illustrated in figure 9(a). Figure 2 shows that linear elasticity is a good match to DFT in the plane of a $\langle 111 \rangle$ dumbbell beyond a separation of a_0 , or about $0.4a_0$ outside the radius $\rho(m=1)$. Varying the minor radius δ of the core region shows that we have a good fit to DFT results for the maximum binding energy $E_b(1\text{H.mSIA})$ in figure 7 if we set $\delta = 0.4a_0$. For a quick indication of the numerical values, the maximum binding energy of the two-shell model can be approximated by $E_b(1\text{H.mSIA}) \approx 0.1069 \log(19.861m)$ eV $\pm 1\%$ for $4 \leq m \leq 50$. Comparison of the two-shell model to the 1H.1SIA binding energies computed by DFT gives a best fit $z_c = 0.8a_0$, which just encloses the most binding sites of figure 1.

The final part of the two-shell model is the short-range H–H pairwise repulsion, which we take as the DFT values +0.47 eV for two H atoms at nearest tetrahedral sites, +0.11 eV for a pair at next nearest tetrahedral sites and zero outside. We have not parameterized octahedral sites, and we neglect many-body interactions. Note that the two-shell model does not consider the enthalpy of formation of the defect or the hydrogen atoms, only the interaction energy in the H + defect system.

With this model, the energy for any system of (idealised) self-interstitial clusters or loops and H atoms on tetrahedral sites can be estimated. The number of H atoms retained on an interstitial defect can be computed at finite temperature by direct computation of the free energy of the $n\text{H.mSIA}$ system, then searching for the equilibrium point where the chemical potential of hydrogen atoms in the interacting hydrogen plus loop system equals the chemical potential of hydrogen in a distant reservoir. The free energy is evaluated using thermodynamic integration [70]. Consider scaling the magnitude of all interactions between H atoms, and between H atoms and

a dislocation loop, with a single parameter $0 \leq \lambda \leq 1$, so that $\lambda = 0$ corresponds to the non-interacting system and $\lambda = 1$ corresponds to the fully-interacting system. The internal energy of a particular microstate s is then $U_\lambda(s) \equiv \lambda U_1(s)$. The partition function $Q_\lambda \sim \sum_s \exp(-\lambda U_1(s)/k_B T)$, and the free energy is $F_\lambda = -k_B T \ln(Q_\lambda)$. Then

$$\frac{\partial F_\lambda}{\partial \lambda} = \frac{\sum U_1 \exp(-\lambda U_1/k_B T)}{\sum \exp(-\lambda U_1/k_B T)} \equiv \langle U_1 \rangle_{T/\lambda}. \quad (7)$$

Integrating this expression gives the fully-interacting free energy $F_1(T)$,

$$\begin{aligned} F_1(T) = F_0(T) &+ \int_{\lambda=0}^1 \langle U_1 \rangle_{T/\lambda} d\lambda = F_0(T) \\ &+ T \int_T^\infty \frac{1}{T'^2} \langle U_1 \rangle_{T'} dT'. \end{aligned} \quad (8)$$

$F_0(T)$ is the free energy in the non-interacting limit, which for n randomly placed hydrogen atoms in a box of N atoms ($6N$ tetrahedral sites) is

$$F_0(n; T) = -k_B T \ln \left(\frac{(6N)!}{(6N-n)!n!} \right). \quad (9)$$

Again, we note that this expression does not include the enthalpy of formation of the hydrogen + defect system.

In order to estimate $\langle U_1 \rangle_{T'}$, and consequently, $F_1(n; T)$, n hydrogen atoms were randomly placed in a box of $N = 30 \times 30 \times 30$ primitive bcc unit cells with periodic boundary conditions and a single loop of size $m \cdot 8 \times 10^5 \times n$ Metropolis steps were taken at each temperature, T' , reducing from 2000 K to 50 K in steps of 50 K, where each Metropolis step considered moving one H atom to an adjacent tetrahedral site. Thirty independent runs were undertaken and the results merged. At the lowest temperature, the H atoms find strongly binding positions. The maximum binding energy for $n\text{H.1SIA}$ is plotted in figure 4(a). The maximum binding energy for 1H.mSIA is plotted in figure 7(b). The lowest energy configuration found for 316H.55SIA is illustrated in figure 9(b).

The chemical potential is $\mu_\lambda(n; T) \equiv F_\lambda(n+1; T) - F_\lambda(n; T)$. For a distant reservoir with a low concentration of hydrogen equal to c_H we can take the non-interacting limit and write $\mu_0(c_H; T) \simeq k_B T \ln c_H$. The chemical potential for

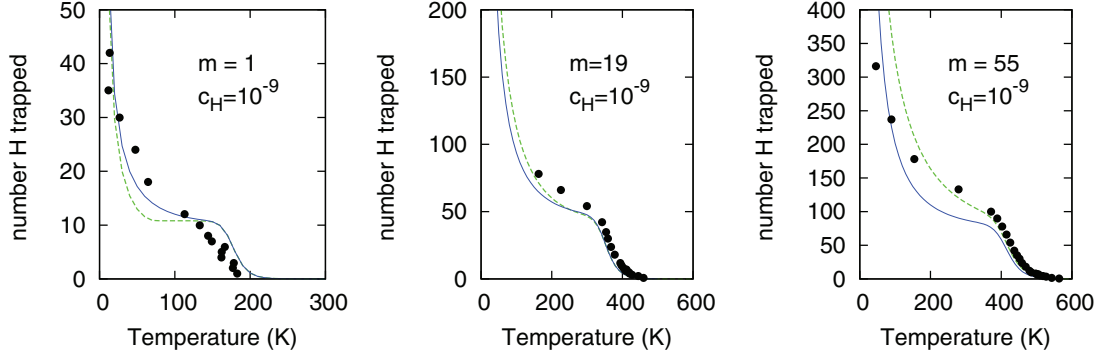


Figure 10. The number of H atoms trapped, on left: by a $\langle 111 \rangle$ dumbbell, centre: by a small $m = 19$ loop, right: by a loop of radius 1 nm ($m = 55$) visible in a transmission electron microscope. Points: matching chemical potentials with a distant reservoir ($c_H = 10^{-9}$) using thermodynamic integration of the two-shell model. Solid lines: numerical integration of equation (10) (see section 3.2). Dashed lines:

an interacting system, $\mu_1(n; T) = F_1(n + 1; T) - F_1(n; T)$, is computed from equation (8). In figure 10 we find the number n of hydrogen atoms in the interacting system which will be in equilibrium with a concentration c_H in a distant reservoir. This number is plotted as a function of temperature.

We see that a $\langle 111 \rangle$ crowdion ($m = 1$) can trap a large cloud of hydrogen atoms at cryogenic temperature, but by room temperature is unlikely to store any hydrogen even in its core region. The increase in entropy gained by releasing hydrogen into the bulk more than outweighs the small binding energy even at modest temperatures. A 2 nm diameter dislocation loop ($m = 55$) can store multiple H atoms up to higher temperatures, provided it is in contact with a high-concentration reservoir. If this reservoir is removed, for example by pumping down the external hydrogen partial pressure in a vacuum chamber under equilibrium conditions, then hydrogen atoms will detrap.

3.2. The Cottrell atmosphere of dislocation loops and edge dislocations

In this section we derive formulae describing the retention of hydrogen by elastic fields of interstitial defects, interstitial loops, and edge dislocations. We provide both numerical estimates and analytical expressions for the number of hydrogen atoms retained by small and large prismatic dislocation loops that are similar to the loops produced by irradiation.

Assuming that once a hydrogen interstitial occupies a certain exclusion volume Ω_H , it is forbidden for other hydrogen atoms to occupy the same volume, the spatially-dependent concentration of hydrogen atoms around an interstitial defect or a dislocation is given by the Fermi distribution [71–73]

$$c(\vec{R}) = \frac{c_H \exp(-U(\vec{R})/k_B T)}{1 + c_H [\exp(-U(\vec{R})/k_B T) - 1]}. \quad (10)$$

Here $U(\vec{R})$ is the energy of interaction between a defect and a hydrogen atom at point \vec{R} , c_H is the asymptotic concentration of hydrogen atoms far away from a defect or a dislocation, defined in terms of the number of hydrogen atoms occupying a unit of the size of exclusion volume Ω_H . The chemical

potential of non-interacting hydrogen atoms in the perfect lattice is $\mu_0 = -k_B T \ln(1/c_H - 1)$, which in the limit of $c_H \ll 1$ can be approximated as $\mu_0 = k_B T \ln(c_H)$ and

$$c(\vec{R}) = \frac{1}{1 + \exp\left(\frac{U(\vec{R}) - \mu_0}{k_B T}\right)}.$$

The maximum concentration of hydrogen corresponds to the case where all the next-nearest-neighbour tetrahedral sites are occupied. Since we can fit six hydrogen atoms into a cubic unit cell of volume $a_0^3 = 2\Omega$, we arrive at the following estimate for the exclusion volume $\Omega_H = \Omega/3$.

Equation (10) shows that iso-surfaces of constant energy are also iso-surfaces of constant equilibrium concentration (see figure 8). In a volume, enclosed by the surface defined by condition $c(\vec{R}) = 1/2$, all the sites available for the occupation by hydrogen are occupied with probabilities higher than 1/2 [72, 73]. Outside this surface the concentration of hydrogen rapidly decreases to the equilibrium asymptotic bulk value $c_H \ll 1$, determined by the experimental boundary conditions. If the volume enclosed by this 1/2 equilibrium concentration, around defect is $V_{c>1/2}$ then the estimate for the number of hydrogen atoms retained by the defect is $N = V_{c>1/2}/\Omega_H$.

We first consider the retention of hydrogen in the core region of a defect or a dislocation. The binding part of the core region (excluding the end caps for simplicity) is a cylinder with inner radius ρ , outer radius $\rho + \delta$ and length $2z_c$, a volume $V_{\text{core}} \simeq 4\pi\rho\delta z_c$. A hydrogen atom within this cylinder has a constant energy U_{core} . The number of hydrogen atoms trapped in the core, per unit length of the dislocation forming the loop perimeter, is therefore

$$n_{\text{core}} = \frac{2\delta z_c}{\Omega_H} \frac{1}{1 + \exp\left(\frac{U_{\text{core}} - \mu_0}{k_B T}\right)}. \quad (11)$$

Outside the core region, equation (4) can be used for computing the energy of interaction, in order to evaluate the trapping volume V_{elas} numerically.

$$V_{\text{elas}} = \int_{\text{exc.core}} \Theta(\mu_0 - U(\vec{R})) d^3\vec{R}, \quad (12)$$

where $\Theta(x)$ is the Heaviside function. We note that the condition $\mu_0 = U(\vec{R})$ is equivalent to $c(\vec{R}) = 1/2$. This surface is analogous to the ‘Fermi surface’ defined in the context of the Thomas–Fermi model for the electronic structure of an atom. Results from numerical integration of equation (12) plus equation (11) are plotted in figure 10 for a (relatively high) equilibrium concentration $c_H = 10^{-9}$. Agreement between the two approaches shows that the estimate for the number of trapped H atoms, obtained by computing the volume enclosed inside a surface defined by condition $c(\vec{R}) = 1/2$, is indeed reasonable.

In what follows, we are going to compute the volume inside the $c(\vec{R}) = 1/2$ iso-surface to derive several analytical estimates of the number of hydrogen atoms retained in the Cottrell atmosphere of dislocation loops and edge dislocation lines. The energy of interaction between a dislocation and a hydrogen interstitial outside the core region of a defect or a dislocation can be evaluated in the infinitesimal hydrogen interstitial defect approximation, in which the hydrogen atom defect in the material is described by an isotropic elastic dipole tensor of the form $P_{ij} = B\Omega_{\text{rel}}^H \delta_{ij}$ [72, 74], resulting in the following equation for the energy of interaction between a hydrogen interstitial defect and the pressure field of a defect or a dislocation

$$U(\vec{R}) = P(\vec{R})\Omega_{\text{rel}}^H, \quad (13)$$

where $P(\vec{R})$ denotes hydrostatic pressure at point \vec{R} . For a small loop, it is necessary to take into account the overlapping regions of negative and positive pressure associated with the opposite sides of the edge dislocation forming the prismatic loop. In our recent paper [74] (see equation (17)), we derived a simple expression which, unlike equation (4), does not require evaluation of elliptic integrals. The distribution of pressure around the loop, in cylindrical polar coordinates (r, θ) , is

$$P(r, \theta) = A \frac{\mu b}{3\pi} \frac{1+\nu}{1-\nu} \frac{3\cos^2(\theta)-1}{2r^3}. \quad (14)$$

where $A = \pi\rho^2$ is the loop area, and θ is the angle to the loop normal. The total volume outside the core region near a small loop, where hydrostatic pressure is negative and is below a certain critical value P_c defined by condition $c(\vec{R}) = 1/2$, is

$$V_{\text{elas}} = 2\pi \int_{\theta_0}^{\theta_1} \sin \theta d\theta \int_{r=r_{\min}}^{r_c(\theta)} r^2 dr. \quad (15)$$

This expression does not describe the toroidal geometry at short distance. Instead we simply match r_{\min} to the exclusion volume of the core region, $\frac{4}{3}\pi r_{\min}^3 \simeq 8\pi\rho\delta z_c$. The critical radius $r_c(\theta)$ is obtained by using equation (14) and the critical pressure $P_c = (k_B/\Omega_{\text{rel}}^H) \ln(c_H)$. Note that P_c is negative since $\Omega_{\text{rel}}^H > 0$ and $c_H \ll 1$. $r_c(\theta)$ determines the spatial extent of the Cottrell atmosphere around the loop. It depends on temperature and increases as a function of hydrogen concentration in the reservoir. A detailed derivation is given in appendix A.

The total number of hydrogen trapped by a small interstitial loop of radius ρ is obtained by adding the number of hydrogen atoms trapped in the core, namely

$$N_{\text{loop}} = 2\pi\rho n_{\text{core}} + \frac{2\pi}{3\Omega_H} \xi_c \left[A \frac{-\Omega_{\text{rel}}^H}{k_B T \ln c_H} \frac{\mu b}{3\pi} \frac{1+\nu}{1-\nu} (1 - \xi_c^2) - 6\rho\delta z_c \right] \quad (16)$$

where $\xi_c^2 = (1/3)(1 - 2r_{\min}^3/(Ax_c))$ and $x_c = -\frac{1}{P_c} \frac{\mu b}{3\pi} \frac{1+\nu}{1-\nu}$. Applications to three loop sizes are illustrated in figure 10.

We now consider the large loop limit. The distribution of hydrostatic pressure around a straight linear edge dislocation in the plane orthogonal to the dislocation line is given, in cylindrical polar coordinates (r, θ) , by the equation [75]

$$P(r, \theta) = \frac{\mu b}{3\pi} \frac{1+\nu}{1-\nu} \frac{\sin \theta}{r}, \quad (17)$$

where θ is the angle with the Burgers vector, with the sign convention that positive angle (and pressure) is in the direction of the half-plane of added interstitials, and the radial distance r is measured from the dislocation line.

For an edge dislocation line of length L , the volume enclosed by the ‘Fermi surface’ outside a core region, where pressure is negative and below the critical value P_c , is again given by an integral

$$V_{\text{elas}} = L \int_{\theta=-\pi}^0 \int_{r=r_{\min}}^{r_c(\theta)} r dr d\theta. \quad (18)$$

Inverting equation (17) gives $r_c(\theta) = x_c \sin \theta$. The integral can be evaluated and matching r_{\min} to the excluded core: $\pi r_{\min}^2/2 \simeq 2\delta z_c$, the resultant number of trapped hydrogen per unit length of an edge dislocation line, being the sum of the core and elastic field contributions, is

$$n_{\text{line}} = n_{\text{core}} + \frac{\pi}{4\Omega_H} \max \left[0, \left(\left(\frac{-\Omega_{\text{rel}}^H}{k_B T \ln c_H} \frac{\mu b}{3\pi} \frac{1+\nu}{1-\nu} \right)^2 - \frac{8\delta z_c}{\pi} \right) \right]. \quad (19)$$

An estimate of the maximum energy of interaction between a hydrogen interstitial atom and an edge dislocation (corresponding to the limit of large loop size) is $U_{\text{core}} = -\frac{1}{\delta} \frac{\mu b}{3\pi} \frac{1+\nu}{1-\nu} \Omega_{\text{rel}}^H = -0.97 \text{ eV}$. This value depends on the two parameters that we determined in this work, $\Omega_{\text{rel}}^H = 0.15\Omega$ and $\delta = 0.4a_0$. The significance of this extrapolation to infinite loop size is not trivial. The value of the binding energy of 0.97 eV is close to the solubility energy of hydrogen in the perfect lattice, suggesting that the energy level of H in an H_2 molecule is similar to the energy of H in the core of a dislocation line at 0 K. We will see the consequence to the solubility of H in W as a function of the density of dislocation lines, but keeping in mind the sensitivity of this value to δ . Indeed, it is just a convenient parameter that positioned the bridge between the atomistic core shell and the elastic shell of our two-shell model, between two distinct tetrahedral sites. Applications of equation (19) for different H concentration in the reservoir are plotted in figure 11.

Comparing figures 10 and 11, we can see that the small loop approximation is adequate for the smallest interstitial defects, the $\langle 111 \rangle$ dumbbell, and good for a TEM visible $m = 55$ ($\rho = 1 \text{ nm}$) loop. The dislocation line approximation is good for larger loops of $m \geq 1400$ ($\rho \geq 5 \text{ nm}$).

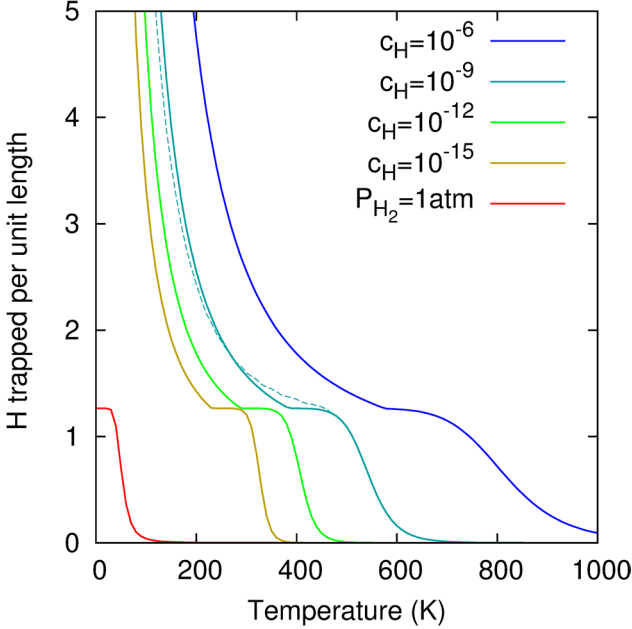


Figure 11. The number of hydrogen atoms retained per unit dislocation line length in equilibrium with hydrogen concentration c_H , or with a partial pressure of H_2 gas above a surface, computed using equation (19). Dashed line shows a numerical integration of the trapping volume (equation (12)) plus core contribution (equation (11)) for $c_H = 10^{-9}$ and $m = 5000$ ($\rho = 10$ nm).

What is notable is the strong temperature dependence of N and also the fact that its magnitude is fairly macroscopic. While the core hydrogen retention is described by a simple Fermi function, the dependence of the elastic field retention on c_H is logarithmic, and so varies relatively insignificantly over a range of bulk hydrogen concentrations spanning many orders of magnitude. Concluding this section, we note that the above treatment only applies to defects that have pressure fields associated with them.

3.3. Solubility

Hydrogen solubility in a metal is defined as the mole fraction of hydrogen atoms to metal atoms at equilibrium, usually presented as a function of temperature and pressure. Equation (19) gives the amount of hydrogen retained per unit length of an edge dislocation in terms of the background hydrogen concentration c_H far away from the dislocation. We therefore need an expression for c_H , which we derive assuming an equilibrium with a perfect gas phase at a partial pressure P above the surface. As justified in appendix B, one has,

$$c_H = \left(\frac{\alpha P}{(k_B T)^{7/2}} \right)^{1/2} \exp \left(-\frac{H^f}{k_B T} + \frac{5}{4} \right), \quad (20)$$

where H^f is the formation enthalpy at 0 K of H inserted in W bcc matrix, α is a constant given in the appendix. The square-root dependence on partial pressure is known as Sievert's law.

Given the dislocation line density ρ_D (measured in inverse area units), the total length of dislocation lines in volume V

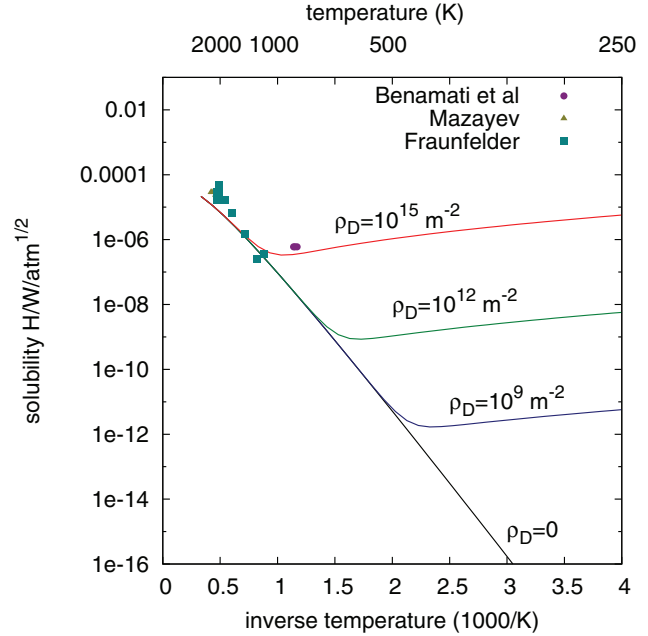


Figure 12. Solubility of hydrogen in tungsten as a function of temperature and dislocation line density for a partial pressure of H_2 gas of 1 atm. Experimental results from [4].

of material is $V\rho_D$, the number of hydrogen atoms trapped on dislocations in volume V is $n_{\text{line}}V\rho_D$ and the solubility is

$$s(T, p, c_H) = \frac{H \text{ on line} + H \text{ in bulk}}{W \text{ in bulk}} = \frac{V\rho_D n_{\text{line}} + 6c_H V/\Omega}{V/\Omega} = \Omega n_{\text{line}}\rho_D + 6c_H, \quad (21)$$

with n_{line} given by equation (19) and c_H by equation (20). The factor of 6 acknowledges the six tetrahedral sites per tungsten atom. The double counting of bulk and elastically trapped sites as the bulk occupation has been neglected. This is plotted in figure 12 for a range of dislocation densities from $\rho_D = 10^{-15}$ to 10^{-9}m^{-2} at a gas pressure $P = 1$ atm of H_2 gas (taking $H^f = 0.95$ eV and $U_{\text{core}} = -0.97$ eV, as previously established), and compared with the experimental results cited in [4]. The high temperature regime can be recognized with the solubility dominated by the occupancy of the sites of the perfect lattice and is in agreement with Frauenfelder's results [3] which gave the solubility expression commonly used for H in W. At low temperature the slope of the solubility reverses because of the sign of $H^f - U_{\text{core}}$. This is a spectacular qualitative effect but we keep in mind that the sign of this energy difference relies on the value taken for δ in our two-shell model whose dependence on loop size has not been established. More importantly, the solubility is larger by order of magnitude because of the trapping in the Cottrell atmospheres of the dislocations. Strictly speaking, our formulae allow the distinction of the contributions of the core and the purely elastic field. In particular, the elastic contribution shrinks for the intermediate temperature range. In W, where the relaxation volume of an H atom is small and its solubility energy H^f large, only the core contribution plays a role under fusion relevant temperature and pressure conditions.

4. Discussion

This study spans atomistic and larger scale models for H atoms interacting with interstitial defects and dislocations in tungsten. The model leads to an analytical expression for hydrogen solubility in tungsten, accounting for the presence of dislocations and defects in the material. In our study we focused on the interstitial type defects and dislocation loops, but to describe the experimental data on irradiated materials one must include vacancy type defects.

At the atomistic scale, we explored a large number of configurations representing interstitial defects of various shapes and sizes, and investigated the accumulation of H on these defects. We found that a hydrogen atom interacts with five W atoms when it is trapped by an interstitial defect, instead of four when it sits in the tetrahedral site of the perfect lattice. Our results show that the strength of interaction is correlated with the H-W distance in the core of the defect, and with hydrogen relaxation volume at larger distances from the core. Our model gives a simple formula for the binding energy of an H atom interacting with a loop of any size, however the model does not take into account the variation of the binding energy around a small loop, an effect particularly evident for an asymmetric loop, such as the 10SIA loop.

The maximum binding energy, found using DFT, of one H atom to a dislocation loop was 0.66 eV, and we expect that larger loops would have the binding energy that is a little larger. Our two-shell model predicts an upper limit of 0.97 eV for the binding energy of hydrogen in the core of an edge dislocation, which we already discussed in detail. As expected, this value is higher than the DFT binding energy of hydrogen to a screw dislocation in bcc W, 0.57 eV. This latter value can be seen as a lower limit of the binding energy of hydrogen to a straight dislocation line. The above values of binding energies of H to edge dislocation, agree well with the maximum trapping energies associated with self-interstitial defects and dislocations, proposed by Ogorodnikova and Sugiyama [27] on the basis of experimental TDS results.

When performing structural relaxations, we observed that a $\langle 111 \rangle$ SIA can easily glide if an H atom is introduced at distances further than $1.5a_0$ from the centre of the crowdion defect. This gliding mode of motion is going to be inhibited if the defect is surrounded by appreciable H atmosphere. For a large loop, it was observed that, in some configurations, a section of the edge of the loop was pinned by an H atom, after a glide that occurred during energy minimization. This highlights the part played by the long range of hydrogen-defect interactions, and the difficulties associated with the definition of the initial and final configurations.

The use of semicore electrons in DFT calculations involving bulk tungsten has an impact on the formation energy of interstitial defects, and influences the binding energy of H atoms, but does not change qualitatively the results presented here. The increase of energy when one moves the interstitial H atom from its tetrahedral position towards one of its nearest W atom, without relaxing atomic positions, is plotted in figure 13, using DFT and EP calculations. The values computed without semicore electrons, labelled ‘DFT’, and with

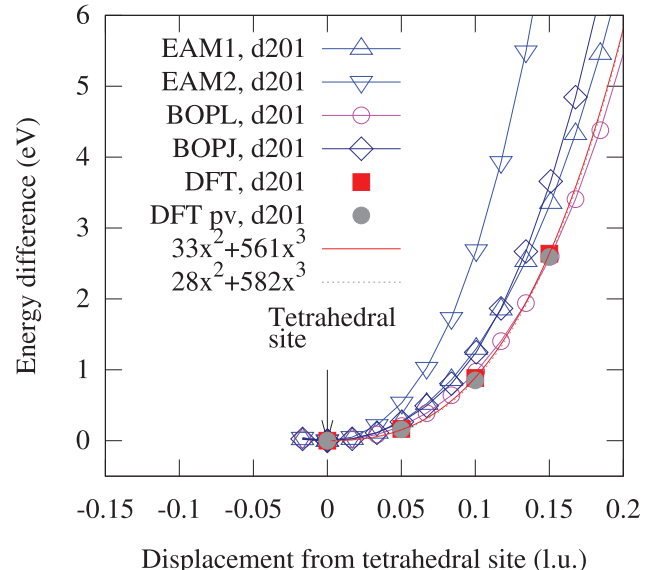


Figure 13. Difference between energies computed dragging an H atom from its interstitial tetrahedral position towards one of its nearest W atoms. Calculations were performed using EP and DFT, with and without semicore electrons included in the electronic structure treatment of W atoms.

semicore electrons, labeled ‘DFTpv’, almost superimpose whereas EAM2 proves stiffer than EAM1, and BOPL is slightly stiffer than BOPJ. The stiffness of the W-H interaction partly correlates with the relaxation volume of an H atom. The DFT relaxation volume value is 0.15Ω . Our study explained why this quantity is important and hence must be reproduced by empirical potentials.

To distinguish between elastic and chemical contributions to the binding energy when H atoms accumulate around a defect, we explored the electronic charge densities. Here, we chose three configurations: a hydrogen-vacancy cluster ($1H.1V$), $1H.1SIA$, and $12H.1SIA$ where the H atoms interact with 5W atoms as opposed to 4W atoms in the perfect lattice. The H-defect distances are similar and the H-H distances are such that their interaction is negligible. The binding energies of the $1H.1SIA$ and the $12H.1SIA$ are related by $E_b(12H.1SIA) \sim 12E_b(1H.1SIA)$ (see equation (2)). The binding energy is mainly *chemical* in origin; we have demonstrated that the linear elasticity is not valid at this short distance. The electronic charge density of the fully relaxed $nH.mSIA$ configurations and the charge densities of m self interstitial and n hydrogen atoms in vacuum have been computed as described in [76]. The positions of the m self interstitial and n hydrogen atoms are the same as their positions in $nH.mSIA$. Then, we define the charge density difference of the deformation of charge density, as

$$\Delta\rho(nH.mSIA) = \rho(nH.mSIA) - \rho(mSIA) - \rho(nH). \quad (22)$$

The charge density differences are represented in planes containing the defect and one or more H atoms in figures 14(a)–(c), respectively for $1H.1V$, $1H.1SIA$ and $12H.1SIA$. The charge density differences show hybridization between *d*-orbitals of the nearest W atoms and the *s*-orbital of the H atom as we

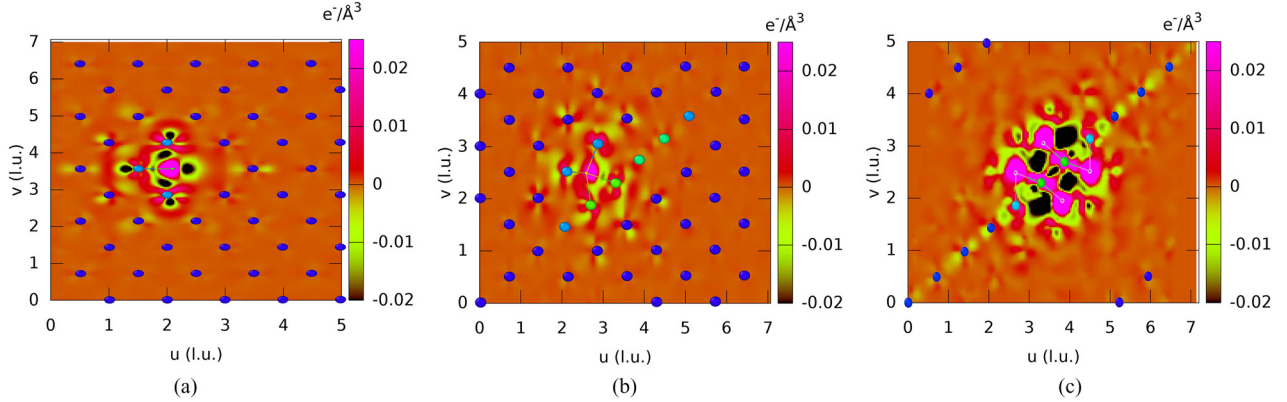
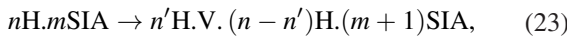


Figure 14. Deformation of charge density defined by equation (22) of (a) the 1H.1VAC (in the $(0\bar{1}1)$ plane) (b) the 1H.1SIA and (c) the 12H.1SIA in a higher index plane parallel to the $\langle 1\bar{1}1 \rangle$ direction and containing one or more H atoms.

described in [77]. In the 1H.1V configuration, the degree of charge density difference is high, suggesting that significant role is played by the electronic (chemical) effects in the large binding energy. In 1H.1SIA, the deformation of charge density is small but the s -orbital of the H atom is deformed towards a W atom of the dumbbell. In 12H.1SIA, the deformation of charge density is large, indicating strong electronic effects. H-W bonds are particularly visible between the H atoms and the W atoms of the dumbbell, each of them being now surrounded by 6H atoms, imposing a trigonal symmetry. On the contrary, the charge density between the W atoms along the $1\bar{1}1$ direction is reduced, suggesting weakening of the W-W bonds that form the self-interstitial dumbbell defect [78].

A pertinent question is whether there is a driving force for trap mutation, i.e. the formation of a vacancy and ejection of a SIA that would increase the interstitial loop size, caused by the presence of trapped hydrogen atoms. This process is known for helium atoms in tungsten [66]. The process is energetically favourable when the vacancy-SIA pair formation energy is counterbalanced by the *total* binding energy of the He atoms in the new vacancy. The binding energy of an additional SIA to an m SIA decreases with the defect size, suggesting that trap mutation is more favourable near a large m SIA. In tungsten, an n He cluster can initiate trap mutation even if no defect is present. Moreover, He atoms attract each other at short distance and spontaneously form clusters whereas H atoms form clusters only in the presence of a defect. It is reasonable to investigate the limit of high hydrogen concentration in the core of m SIA defects in a similar manner to the study of the screw dislocation in [13]. We shall now make an estimate for the trap mutation energy at 0K as a function of interstitial defect size. We find that, contrary to an intuitive argument, trap mutation is not energetically favourable.

We describe the trap mutation process as a chemical reaction, namely



that we simplify by assuming $n = n'$. This chemical reaction can be virtually decomposed as the following sequence of steps with the corresponding evolution of the system energy,

$$\begin{array}{lll} nH.mSIA & \rightarrow & nH + mSIA \\ mSIA & \rightarrow & (m+1)SIA + 1V \\ nH + V & \rightarrow & nH.1V \\ nH.1V + (m+1)SIA & \rightarrow & nH.1V.(m+1)SIA \\ nH.mSIA & \rightarrow & nH.1V.(m+1)SIA \end{array} \quad \begin{array}{l} E_b(nH.mSIA) > 0 \\ \Delta E_{SIA}(m) + E_f(V) > 0 \\ -E_b(nH.1V) < 0 \\ -\Delta E_c \\ E_{tm} \end{array} \quad (24)$$

where

$$\Delta E_{SIA}(m) = E_f((m+1)SIA) - E_f(mSIA) > 0 \quad (25)$$

is the formation energy of an additional SIA joining the loop, which decreases with loop size. $E_b(nH.mSIA)$ is the binding energy of H to the loop, as estimated in this work, which increases with loop size. $E_b(nH.1V)$ is the binding energy of H atoms in a vacancy and ΔE_c is the binding energy of the $nH.1V$ complex formed in close proximity to the loop. If E_{tm} is negative, there is a driving force for trap mutation at low temperature. For the formation energy of a m SIA loop, we use the empirical formula that we established in [79] and for the formation energy of a hydrogen-decorated vacancy, we use results of [5, 45]. Everywhere the values do not include the ZPE correction to retain consistency of the approach.

We also calculated the formation energies of various $nH.mSIA$ and $nH.1V.(m+1)SIA$ complexes with empirical potentials using a $2000 \times 2000 \times 2000$ cell box. 6H atoms and one 6H.1V were introduced into the core of various m SIA loops. As an example, we consider the case of a 89SIA loop. A 90SIA loop was obtained starting from a prismatic 91SIA loop and removing one dumbbell from a corner, and then a 89SIA was obtained by removing also a dumbbell closest to the loop edge. 6H atoms were introduced in the tetrahedral sites around the missing dumbbells in order to form a 6H.89SIA, and a 6H.1V was placed in a corner to form a 6H.1V.90SIA. Local energy minima were sought by first relaxing the structure using conjugate gradients, and then ramping up temperature from 0K to 200K and back over 10ps of MD, then relaxing again. Formation energies of complexes are given in table 4 together with the comparison with our model based on DFT calculations. We see that DFT calculations, EAM1 and EAM2 do not predict trap mutation, but that BOPL might, owing to the overestimation of the binding energy of 6H to one vacancy.

Table 4. Contributions to the trap mutation energy (in eV), obtained using EPs and our model based on DFT calculations.

Energy	EAM1	EAM2	BOPL	Model
$E_b(6\text{H.89SIA})$	2.14	4.40	4.43	4.80*
$E_f(90\text{SIA}) - E_f(89\text{SIA})$	1.52	1.52	1.37	1.80 ^a
$E_f(\text{V})$	3.49	3.49	3.52	3.31
$E_b(6\text{H.V})$	3.39	4.81	10.43	6.08
$E_b(\text{V.90SIA})$	1.40	0.37	0.83	1.97 ^a
E_{tm}	2.36	4.23	-1.94	1.83

^a The formation energy of the $1/2\langle 111 \rangle$ loops are from [79] and binding energies are calculated using our TS model.

The explanation is that the energy gain of trapping H in a vacancy is offset by the H binding energy to the loop, and so never outweighs the formation energy of the vacancy and SIA, even though the last one decreases with the loop size. Missing from this analysis is the effect of finite temperature. We have found that the vacancy + loop complex is metastable, which means there will be some thermal activation barrier for trap mutation, which we have not attempted to find. At finite temperatures we find that the equilibrium occupation of trapping sites is typically low, which decreases the likelihood of trap mutation occurring.

5. Conclusion

We have presented a comprehensive multiscale study of the interaction between hydrogen and interstitial defects and dislocations in tungsten, using the density functional theory, the linear elasticity theory and empirical potentials to justify and parameterize a simplified pairwise model and from there to derive and validate analytical formulae for hydrogen retention and solubility in tungsten.

In section 2.1 we found that the binding energy of one hydrogen atom to a single SIA in the form of a $\langle 111 \rangle$ dumbbell is 0.3 eV, in agreement with our previous studies, and that the binding energy of n hydrogen atoms to a single SIA increases linearly up to $n = 12$. We showed that the short range repulsion between two hydrogen atoms in tungsten also applies when H atoms accumulate around an interstitial defect. Our model then assumes that the interaction of hydrogen with interstitial-type defects is the summation of pairwise interactions only. The hybridization between s -orbitals of hydrogen atoms and d -orbitals on the neighbouring tungsten atoms has been illustrated by computing the deformation charge densities. We concluded that the binding energy in the core of defects is due to the hydrogen atom having 5 nearest W neighbours, whereas the number of nearest W atoms in a perfect lattice is 4.

We showed that at long range (greater than one lattice parameter away from the atoms forming the core of an interstitial cluster or a dislocation), the interaction between a hydrogen interstitial atom and a defect or a dislocation is well described by linear elasticity. The maximum binding energy of a hydrogen atom to an interstitial cluster or a dislocation loop increases with loop size. DFT calculations gave the maximum binding energy of 0.66 eV for a hydrogen atom to a $m = 37$ SIA loop. The binding energy of hydrogen in the core of an

edge dislocation, according to the two-shell model, is 0.97 eV. These values can be considered as the lower and upper limits of hydrogen binding energies characterizing edge dislocation. These values can be directly compared to the range of trapping energies associated with self-interstitial defects and dislocations (0.4–0.8 eV), proposed by Ogorodnikova and Sugiyama [27] on the basis of experimental TDS data. In section 3.1 we described a two-shell pairwise model for hydrogen-interstitial loop interaction which we then used in Metropolis Monte Carlo simulations and for thermodynamic integration. We conclude that at high background hydrogen concentration, hydrogen is trapped in the dislocation core and by the tensile elastic fields in the vicinity of defects and dislocations.

We simplified the pairwise model to provide analytical formulae describing hydrogen Cottrell atmospheres of dislocation loops and line dislocations, and their contributions to the hydrogen solubility in tungsten at elevated temperatures. We find that under fusion relevant conditions (hydrogen gas partial pressure of 1 atm), only a tiny amount of hydrogen would be retained on dislocations or interstitial defects in tungsten. We can identify three regimes of hydrogen solubility, corresponding to trapping of hydrogen by elastic fields and dislocation cores at low temperature/high background concentration, trapping at dislocation cores only at intermediate temperature/concentration, and no trapping at high temperature/low background concentration.

Analysing molecular statics and analytical extrapolations, we proved that trap mutation does not occur spontaneously on interstitial defects of any size at 0 K.

The above analysis helps understand hydrogen interaction with dislocations and interstitial defects in tungsten under conditions where high H concentration is observed in the subsurface layer during tungsten exposure to a high flux plasma. The general methodology presented here, and the analytical formulae derived, are likely to be applicable to other metals and other types of impurities, for example nitrogen or carbon.

Acknowledgments

This work was part-funded by the RCUK Energy Programme [grant number EP/P012450/1]. This work has been carried out within the framework of the EUROfusion Consortium and has received funding from the Euratom research and training programme 2014–2018 under grant agreement No 633053. The views and opinions expressed herein do not necessarily reflect those of the European Commission. This work was supported by EUROfusion Enabling Research project TriCEM, *Tritium Retention in Controlled and Evolving Microstructure*, and JET3_TRI project. M.-C. Marinica acknowledges support from the GENCI -(CINES/CCRT) computer centre under Grant No. A0010906973. Most of atomic structures shown in figures have been generated using Ovito [80].

Appendix A. Calculation of the volume enclosed by the ‘Fermi surface’ around a dislocation loop

Using the volume element $dV = 2\pi r^2 dr \sin \theta d\theta$, the total volume outside the core region ($r > r_{\min}$) near a small loop

where pressure is negative and is below a certain critical value P_c equals

$$V_{\text{elas}} = 2\pi \int_{\theta_0}^{\theta_1} \sin \theta d\theta \int_{r=r_{\min}}^{r_c(\theta)} r^2 dr = \frac{2\pi}{3} \int_{\theta_0}^{\theta_1} (r_c^3(\theta) - r_{\min}^3) \sin \theta d\theta, \quad (\text{A.1})$$

where we find r_{\min} by matching the excluded volume in the core volume $\frac{4}{3}\pi r_{\min}^3 \simeq 8\pi\rho\delta z_c$. From equation (14) we find

$$\begin{aligned} r_c^3(\theta) &= \max \left[r_{\min}^3, -\frac{A}{P_c} \frac{\mu b}{3\pi} \frac{1+\nu}{1-\nu} \frac{1-3\cos^2\theta}{2} \right] \\ &= \max \left[r_{\min}^3, Ax_c \frac{1-3\cos^2\theta}{2} \right], \end{aligned} \quad (\text{A.2})$$

where we defined a positive length constant $x_c = -\frac{1}{P_c} \frac{\mu b}{3\pi} \frac{1+\nu}{1-\nu}$. The integration spans the interval where $0 < \cos^2\theta < \xi_c^2 = (1/3)(1 - 2r_{\min}^3/(Ax_c))$. The volume is

$$V_{\text{elas}} = \frac{2\pi}{3} \xi_c [Ax_c(1 - \xi_c^2) - 2r_{\min}^3]. \quad (\text{A.3})$$

Finally we need the value of the critical pressure P_c . We write

$$\frac{1}{2} \{1 + c_H [\exp(-P_c \Omega_{\text{rel}}^H/k_B T) - 1]\} = c_H \exp(-P_c \Omega_{\text{rel}}^H/k_B T). \quad (\text{A.4})$$

Since $c_H \ll 1$ and hence $\exp(-P_c \Omega_{\text{rel}}^H/k_B T) \gg 1$, we find that the condition $c = 1/2$ can be written in the form

$$c_H \exp(-P_c \Omega_{\text{rel}}^H/k_B T) = 1. \quad (\text{A.5})$$

From this equation, we find the critical pressure required to retain a hydrogen atom by the elastic field (which is negative since the relaxation volume of a hydrogen interstitial atom is positive)

$$P_c = -\frac{k_B T}{\Omega_{\text{rel}}^H} \ln(1/c_H). \quad (\text{A.6})$$

Appendix B. H chemical potential of the diatomic hydrogen gas

At temperatures relevant for fusion materials ($T < 2000$ K), the molecular partition function of a diatomic hydrogen gas is

$$q = q_{\text{trans}} \cdot q_{\text{rot}} = \frac{V}{\Lambda^3} \frac{k_B T}{2B}, \quad (\text{B.1})$$

where $\Lambda = \hbar\sqrt{2\pi/(Mk_B T)}$ is the de Broglie thermal wavelength, $B = \hbar^2/2I$ is the rotational energy scale with $I = d^2 M/2$ is the moment of inertia of a molecule with M the mass of the hydrogen atom and $d = 0.741$ Å the bond length of a diatomic molecule [81]. We do not need to consider the vibrational contribution for hydrogen gas, as the characteristic vibrational temperature is in the range 3200 K to 6800 K for H_2 and 2600 K to 4000 K for D_2 , depending on the pressure and temperature: the lower range is appropriate for a fusion plasma and the upper range more appropriate for low laboratory pressures and temperatures [82]. For a perfect gas of n indistinguishable molecules, the total number of microstates

is approximately $q_{\text{tot}} = q^n/n!$, and so, using Stirling's approximation, the entropy of the gas is

$$S = k_B \ln q_{\text{tot}} \simeq -nk_B \left[\ln \left(\alpha \frac{P}{(k_B T)^{7/2}} \right) + 1 \right]. \quad (\text{B.2})$$

where $\alpha = (2\pi)^{3/2} \hbar^5 / (\sqrt{2} d^2 M^5) = (1/m^5) \times 2.30 \times 10^{-5}$ eV^{5/2} Å³ is a constant for hydrogenic gases, with m the atomic mass of the isotope in Dalton units. The chemical potential of the hydrogen diatomic gas is therefore

$$\mu_{H_2,\text{gas}}(P; T) = k_B T \left(\frac{5}{2} + \ln \left(\frac{\alpha P}{(k_B T)^{7/2}} \right) \right), \quad (\text{B.3})$$

and the chemical potential of hydrogen atoms dissolved in tungsten and in equilibrium with this gas is $\mu_{H,\text{tet}}(c_H; T) = 1/2 \mu_{H_2,\text{gas}}(P; T)$. If we take into account the formation enthalpy, $\mu_{H,\text{tet}}(c_H; T) \simeq H^f + k_B T \ln c_H$. (Note that in the main text our expression for μ_0 only considered the configurational entropy.) We therefore have an expression for the concentration of hydrogen in distant bulk sites in solid tungsten

$$c_H = \left(\frac{\alpha P}{(k_B T)^{7/2}} \right)^{1/2} \exp \left(-\frac{H^f}{k_B T} + \frac{5}{4} \right). \quad (\text{B.4})$$

The square-root dependence on partial pressure is known as Sievert's law. We take $H^f = 0.95$ eV, the DFT computed value without ZPE corrections [5, 45].

References

- [1] Lipschultz B. et al 2010 *Technical Report* MIT, PSFC/RR-10-4
- [2] Fowler R.H. and Smithells C.J. 1937 *Proc. R. Soc. A* **160** 37
- [3] Frauenfelder R. 1969 *J. Vac. Sci. Technol.* **6** 388
- [4] Skinner C.H. et al 2008 *Fusion Sci. Technol.* **54** 891
- [5] Heinola K., Ahlgren T., Nordlund K. and Keinonen J. 2010 *Phys. Rev. B* **82** 094102
- [6] Wróbel J.S., Nguyen-Manh D., Kurzydowski K.J. and Dudarev S.L. 2017 *J. Phys.: Condens. Matter* **29** 145403
- [7] Shimada M., Hatano Y., Calderoni P., Oda T., Oya Y., Sokolov M., Zhang K., Cao G., Kolasinski R. and Sharpe J.P. 2011 *J. Nucl. Mater.* **415** S667
- [8] Falconer J.L. and Madix R.J. 1975 *Surf. Sci.* **48** 393
- [9] Kirchheim R. 2004 *Solid State Physics* ed H. Ehrenreich and F. Spaepen (Amsterdam: Elsevier) p 203
- [10] Hayward E., Hayward R. and Fu C.-C. 2016 *J. Nucl. Mater.* **476** 36
- [11] Yi X., Sand A.E., Mason D.R., Kirk M.A., Roberts S.G., Nordlund K. and Dudarev S.L. 2015 *Europhys. Lett.* **110** 36001
- [12] Sand A.E., Mason D.R., De Backer A., Yi X., Dudarev S.L. and Nordlund K. 2017 *Mater. Res. Lett.* **5** 357
- [13] Terentyev D., Dubinko V., Bakaev A., Zayachuk Y., Renterghem W.V. and Grigorev P. 2014 *Nucl. Fusion* **54** 042004
- [14] Terentyev D., De Temmerman G., Morgan T.W., Zayachuk Y., Lambrinou K., Minov B., Dubinko A., Bystrov K. and van Oost G. 2015 *J. Appl. Phys.* **117** 083302
- [15] Grigorev P., Terentyev D., Bonny G., Zhurkin E.E., van Oost G. and Noterdaeme J.-M. 2017 *J. Nucl. Mater.* **465** 364

- [16] Grigorev P., Bakaev A., Terentyev D., van Oost G., Noterdaeme J.-M. and Zhurkin E.E. 2017 *Nucl. Instrum. Methods B* **393** 164 (*Computer Simulation of Radiation effects in Solids Proc. of the 13 Cosires (Loughborough, UK, 19–24 June 2016)*)
- [17] Ramasubramanian A., Mitsuhiro I. and Carter E.A. 2009 *Phys. Rev. B* **79** 174101
- [18] Zhao Y. and Lu G. 2011 *Modelling Simul. Mater. Sci. Eng.* **19** 065004
- [19] Castaño Rivera P., De Vincentis N.S., Bolmaro R.E. and Buzzoni P. 2015 *Proc. Mater. Sci.* **8** 1031
- [20] Lawler H.M. and Trinkle D.R. 2010 *Phys. Rev. B* **82** 172101
- [21] Clouet E., Garruchet S., Nguyen H., Perez M. and Becquart C.S. 2008 *Acta Mater.* **56** 3450
- [22] Kirchheim R. 2007 *Acta Mater.* **55** 5129
- [23] Kirchheim R. 2007 *Acta Mater.* **55** 5139
- [24] Kirchheim R. 2012 *Scripta Mater.* **67** 767
- [25] Itakura M., Kaburaki H., Yamaguchi M. and Okita T. 2013 *Acta Mater.* **61** 6857
- [26] Becquart C.S. and Domain C. 2009 *J. Nucl. Mater.* **386** 109
- [27] Ogorodnikova O.V. and Sugiyama K. 2013 *J. Nucl. Mater.* **442** 518
- [28] Zayachuk Y., 't Hoen M.H.J., Zeijlmans van Emmichoven P.A., Uytdenhouwen I. and van Oost G. 2012 *Nucl. Fusion* **52** 103021
- [29] Jia Y.Z., De Temmerman G., Luo G.N., Xu H., Li C., Fu B. and Liu W. 2015 *J. Nucl. Mater.* **457** 213
- [30] Manhard A. et al 2017 *Nucl. Mater. Energy* accepted
- [31] Grigorev P., Terentyev D., Dubinko V., Bonny G., van Oost G., Noterdaeme J.-M. and Zhurkin E.E. 2015 *Nucl. Instrum. Methods B* **352** 96
- [32] Yang X. and Hassanein A. 2013 *J. Nucl. Mater.* **434** 1
- [33] Ogorodnikova O.V., Markelj S. and von Toussaint U. 2016 *J. Appl. Phys.* **119** 054901
- [34] Shimada M. et al 2012 *Fusion Eng. Des.* **87** 1166
- [35] Marian J. et al 2017 *Nucl. Fusion* **57** 092008
- [36] Založník A., Markelj S., Schwarz-Selinger T., Ciupiński L., Grzonka J., Vavpetič P. and Pelicon P. 2016 *Phys. Scr. T* **167** 014031
- [37] Merrill B.J., Shimada M. and Humrickhouse P.W. 2013 *J. Plasma Fusion Res.* **10** 71
- [38] Shimada M., Hara M., Otsuka T., Oya Y. and Hatano Y. 2015 *J. Nucl. Mater.* **463** 1005
- [39] Ferroni F., Yi X., Arakawa K., Fitzgerald S.P., Edmondson P.D. and Roberts S.G. 2015 *Acta Mater.* **90** 380
- [40] Ahlgren T., Heinola K., Vörter K. and Keinonen J. 2012 *J. Nucl. Mater.* **427** 152
- [41] Hodille E.A., Ferro Y., Fernandez N., Becquart C.S., Angot T., Layet J.M., Bisson R. and Grisolia C. 2016 *Phys. Scr. T* **167** 014011
- [42] Schmid K., von Toussaint U. and Schwarz-Selinger T. 2014 *J. Appl. Phys.* **116** 134901
- [43] von Toussaint U., Schwarz-Selinger T. and Schmid K. 2015 *J. Nucl. Mater.* **463** 1075
- [44] Ohsawa K., Goto J., Yamakami M., Yamaguchi M. and Yagi M. 2010 *Phys. Rev. B* **82** 184117
- [45] Johnson D.F. and Carter E.A. 2010 *J. Mater. Res.* **25** 315
- [46] Fernandez N., Ferro Y. and Kato D. 2015 *Acta Mater.* **94** 307
- [47] Kato D., Iwakiri H., Watanabe Y., Morishita K. and Muroga T. 2015 *Nucl. Fusion* **55** 083019
- [48] Guerrero C., González C., Iglesias R., Perlado J.M. and González-Arrabal R. 2016 *J. Mater. Sci.* **51** 1445
- [49] Bonny G., Grigorev P. and Terentyev D. 2014 *J. Phys.: Condens. Matter* **26** 485001
- [50] Li X., Liu Y., Yu Y., Niu G., Luo G. and Shu X. 2015 *Plasma Sci. Technol.* **17** 524
- [51] Cusentino M., Hammond K.D., Sefta F., Juslin N. and Wirth B.D. 2015 *J. Nucl. Mater.* **463** 347
- [52] Becquart C.S., Domain C., Sarkar U., De Backer A. and Hou M. 2010 *J. Nucl. Mater.* **403** 75
- [53] Markelj S., Schwarz-Selinger T., Založník A., Kelemen M., Vavpetič P., Pelicon P., Hodille E. and Grisolia C. 2016 *Nucl. Mater. Energy*
- [54] Takai K. and Shoda H. 2010 *Matería* **15** 267
- [55] Ahlgren T. and Bukonte L. 2016 *J. Nucl. Mater.* **479** 195
- [56] Cottrell A.H. and Bilby B.A. 1949 *Proc. Phys. Soc. A* **62** 49
- [57] Domain C. and Becquart C.S. 2005 *Phys. Rev. B* **71** 214109
- [58] Kresse G. and Hafner J. 1993 *Phys. Rev. B* **47** 558
- [59] Perdew J. P., Burke K. and Ernzerhof M. 1996 *Phys. Rev. Lett.* **77** 3865
- [60] Varvenne C., Bruneval F., Marinica M.-C. and Clouet E. 2013 *Phys. Rev. B* **88** 134102
- [61] Plimpton S. 1995 *J. Comput. Phys.* **117** 1
- [62] Juslin N., Erhart P., Träskelin P., Nord J., Henriksson K.O.E., Nordlund K., Salonen E. and Albe K. 2005 *J. Appl. Phys.* **98** 123520
- [63] Li X.-C., Shu X., Liu Y.-N., Gao F. and Lu G.-H. 2011 *J. Nucl. Mater.* **408** 12
- [64] Marinica M.-C., Ventelon L., Gilbert M.R., Proville L., Dudarev S.L., Marian J., Benceteux G. and Willaime F. 2013 *J. Phys.: Condens. Matter* **25** 395502
- [65] Hofmann F., Nguyen-Manh D., Gilbert M.R., Beck C.E., Eliason J.K., Maznev A.A., Liu W., Armstrong D.E.J., Nelson K.A. and Dudarev S.L. 2015 *Acta Mater.* **89** 352
- [66] Boisse J., De Backer A., Domain C. and Becquart C.S. 2014 *J. Mater. Res.* **29** 2374
- [67] Baštecká J. and Kroupa F. 1964 *Cechoslovackij Fiziceskij Z. B* **14** 443
- [68] Cai W., Arsenlis A., Weinberger C.R. and Bulatov V.V. 2006 *J. Mech. Phys. Solids* **54** 561
- [69] Lazar M. and Maugin G.A. 2006 *Proc. R. Soc. Lond. A* **462** 3465
- [70] Frenkel D. and Smit B. 2001 *Understanding Molecular Simulation* 2nd edn (New York: Academic)
- [71] Beshers D.N. 1958 *Acta Metall.* **6** 521
- [72] Hirth J.P. and Carnahan B. 1978 *Acta Metall.* **26** 1795
- [73] Dudarev S.L. 2013 *Annu. Rev. Mater. Res.* **43** 35
- [74] Dudarev S.L. and Sutton A.P. 2017 *Acta Mater.* **125** 425
- [75] Heald P.T. and Speight M.V. 1975 *Acta Metall.* **23** 1389
- [76] Domain J.F.C. and Becquart C.S. 2004 *Phys. Rev. B* **69** 144112
- [77] Nakamura H., Nguyen-Manh D. and Pettifor D.G. 2000 *J. Alloys Compd.* **306** 113
- [78] Nguyen-Manh D., Horsfield A.P. and Dudarev S.L. 2006 *Phys. Rev. B* **73** 020101
- [79] Alexander R., Marinica M.-C., Proville L., Willaime F., Arakawa K., Gilbert M.R. and Dudarev S.L. 2016 *Phys. Rev. B* **94** 024103
- [80] Stukowski A. 2010 *Modelling Simul. Mater. Sci. Eng.* **18** 015012
- [81] Haynes W.M. 2016 *CRC Handbook of Chemistry and Physics* 97th edn (Boca Raton, FL: CRC press)
- [82] Fantz U. and Heger B. 1998 *Plasma Phys. Control. Fusion* **40** 2023